

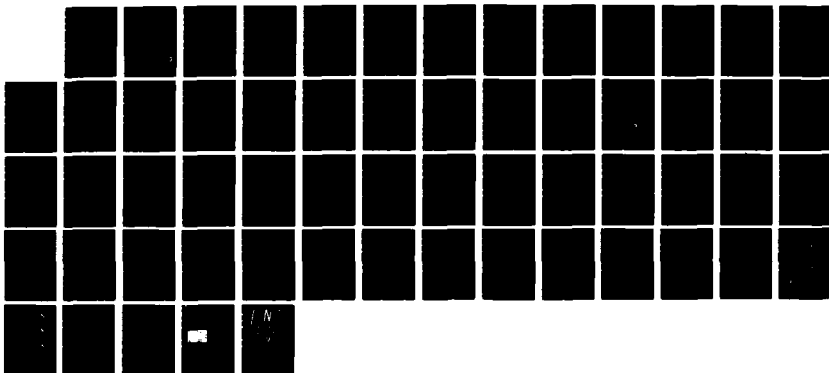
AD-A191 546

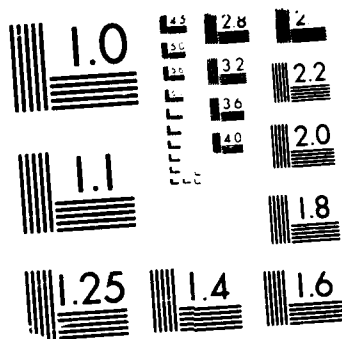
THEORETICAL INVESTIGATION OF 3-D SHOCK WAVE-TURBULENT
BOUNDARY LAYER INTE (U) RUTGERS - THE STATE UNIV NEW
BRUNSWICK NJ DEPT OF MECHANICAL A D D KNIGHT JAN 88
RU-TR-171-MAE-F AFOSR-TR-88-0127 F/G 20/4

1/1

UNCLASSIFIED

NL





MICROCOPY RESOLUTION TEST CHART
 U.S. GOVERNMENT PRINTING OFFICE: 1963 O 454-001

AD-A191 546

Department of Mechanical and Aerospace Engineering
Rutgers University - The State University of New Jersey
New Brunswick, NJ 08903

Report RU-TR-171-MAE-F

*Theoretical Investigation of
3-D Shock Wave-Turbulent Boundary Layer Interactions
Part VI*

Doyle D. Knight

Interim Report for Period 1 October 1986 to 30 September 1987
Approved for Public Release - Distribution Unlimited

Air Force Office of Scientific Research
Building 410
Bolling AFB
Washington, DC 20332

January 1988

DTIC
ELECTE
FEB 29 1988
S D
COH

REPORT DOCUMENTATION PAGE

1a. REPORT SECURITY CLASSIFICATION Unclassified			1b. RESTRICTIVE MARKINGS		
2a. SECURITY CLASSIFICATION AUTHORITY			3. DISTRIBUTION / AVAILABILITY OF REPORT Approved for Public Release Distribution Unlimited		
2b. DECLASSIFICATION / DOWNGRADING SCHEDULE					
4. PERFORMING ORGANIZATION REPORT NUMBER(S) RU-TR-171-MAE-F			5. MONITORING ORGANIZATION REPORT NUMBER(S) A1AFOSR OTR-88-01127 Research		
6a. NAME OF PERFORMING ORGANIZATION Dept. Mech. and Aero. Engr Rutgers University		6b. OFFICE SYMBOL (If applicable)	7a. NAME OF MONITORING ORGANIZATION Air Force Office of Scientific Research		
6c. ADDRESS (City, State, and ZIP Code) PO Box 909 Piscataway, NJ 08855-0909			7b. ADDRESS (City, State, and ZIP Code) Building 410 Bolling AFB Washington, DC 20332		
8a. NAME OF FUNDING / SPONSORING ORGANIZATION Air Force Office of Scien. Res		8b. OFFICE SYMBOL (If applicable) AFOSR/NA	9. PROCUREMENT INSTRUMENT IDENTIFICATION NUMBER AFOSR-86-0266A		
8c. ADDRESS (City, State, and ZIP Code) Building 410 Bolling AFB Washington, DC 20332			10. SOURCE OF FUNDING NUMBERS		
			PROGRAM ELEMENT NO. 6110-1	PROJECT NO.	TASK NO.
11. TITLE (Include Security Classification) Theoretical Investigation of 3-D Shock Wave-Turbulent Boundary Layer Interactions Part VI					
12. PERSONAL AUTHOR(S) Doyle Knight					
13a. TYPE OF REPORT Interim ADNAVAL		13b. TIME COVERED FROM 86/10/1 TO 87/9/30		14. DATE OF REPORT (Year, Month, Day) 88/1/25	
15. PAGE COUNT					
16. SUPPLEMENTARY NOTATION					
17. COSATI CODES			18. SUBJECT TERMS (Continue on reverse if necessary and identify by block number)		
FIELD	GROUP	SUB-GROUP	High speed flows; viscous-inviscid interactions; shock-boundary layer interactions; computational fluid dynamics; Navier-Stokes equations; turbulence		
19. ABSTRACT (Continue on reverse if necessary and identify by block number) The research concerns the understanding of 3-D shock wave-turbulent boundary layer interactions. The research activity has focused on several areas. First, the 3-D swept compression corner has been computed at Mach 3 for a sweep angle of 40 deg and compression angle of 24 deg. The calculated flows are in good agreement with experiment. Second, the flowfield structure of the 3-D swept compression corner is dominated by a large vortical structure. Third, the interaction has been found quantitatively to be dominated by inviscid effects except within a small fraction of the boundary layer. Fourth, the effect of boundary layer bleed has been examined for the 3-D shock wave-turbulent boundary layer interaction generated by a sharp fin. The effects of bleed are principally limited to the near surface region. The overall vortical structure is insensitive to surface bleed.					
20. DISTRIBUTION / AVAILABILITY OF ABSTRACT <input type="checkbox"/> UNCLASSIFIED/UNLIMITED <input checked="" type="checkbox"/> SAME AS RPT. <input type="checkbox"/> DTIC USERS			21. ABSTRACT SECURITY CLASSIFICATION Unclassified		
22a. NAME OF RESPONSIBLE INDIVIDUAL			22b. TELEPHONE (Include Area Code)		22c. OFFICE SYMBOL

PREFACE

This report presents the research accomplishments for FY87 (1 October 1986 to 30 September 1987) of the research investigation entitled "Theoretical Investigation of Three-Dimensional Shock-Wave Turbulent Boundary Layer Interactions".

The research has benefited from the assistance of several individuals, including Drs. James Wilson and Jim McMichael (Air Force Office of Scientific Research), Dr. C. Horstman (NASA Ames Research Center), and Dr. James Keller and Mr. Manuel Salas (NASA Langley Research Center). The interactions with S. Bogdonoff, D. Dolling, A. Ketchum, and G. Settles are acknowledged.



Accession For	
NTIS GRA&I	<input checked="checked" type="checkbox"/>
DTIC TAB	<input type="checkbox"/>
Unannounced	<input type="checkbox"/>
Justification	
By	
Distribution/	
Availability Codes	
Avail and/or	
Dist	Special
A-1	

Table of Contents

Section I. Objectives	4
Section II. Research Accomplishments for FY87 and Research Program for FY88	6
A. Research Accomplishments for FY87	6
B. Research Program for FY88	11
Section III. Publications and Scientific Interactions	16
A. Written Publications - Cumulative Chronological Index	16
B. Visitors to Rutgers University	17
C. Spoken Papers Presented at Technical Meetings	18
D. Seminars	18
Section IV. List of Personnel and Degrees Awarded	19
Section V. References	20
Section VI. Papers	25
"Supersonic Flow Past a 3-D Swept Compression Corner at Mach 3 : Part II"	25
"Numerical Experiments on the 3-D Shock Wave-Boundary Layer Interaction Gen- erated by a Sharp Fin"	25

Section I. Objectives

The principal objectives of the research program are :

1. Develop and Validate Theoretical Model(s) for 3-D Shock Wave - Turbulent Boundary Layer Interaction

The understanding of complex 3-D shock wave-turbulent boundary layer interactions ("3-D turbulent interactions") requires the development and validation of accurate theoretical models. A wide range of theoretical approaches have been employed, extending from simplified control volume analyses (Paynter 1980)* to the Reynolds-averaged three-dimensional compressible Navier-Stokes equations (Horstman and Hung 1979; Knight 1984a, 1984b, 1985a; Knight et al 1986) with turbulence incorporated through a turbulent eddy viscosity model. The present research effort has utilized the algebraic turbulent eddy viscosity of Baldwin and Lomax (1978). The equations are solved numerically using a hybrid explicit-implicit numerical algorithm developed by the present investigator (Knight 1984a). The validation is achieved by comparison of computed and experimental results for 3-D turbulent interactions in simplified geometries. This validation has been a continuous element of the research.

2. Determine the Physical Structure of 3-D Turbulent Interactions for Selected Geometries

A second objective is the determination of the physical flowfield structure of 3-D turbulent interactions in simplified geometries (e.g., 3-D sharp fin [Fig. 1] and 3-D swept compression corner [Fig. 2]). This understanding is naturally linked to the development and verification of accurate theoretical model(s) for 3-D turbulent interactions, and as such requires a coordinated effort between theory and experiment. During FY85** the collaboration of C. C. Horstman (NASA Ames Research), B. Shapey and S. Bogdonoff (Princeton) and the author led to an understanding of the flowfield structure of the 3-D sharp fin configuration (Knight et al 1987a). During FY86, a similar collaboration led to the understanding of the flowfield structure for the 3-D swept compression corner at Mach 3 for $(\alpha, \lambda) = (24, 60)$ deg. During FY87, the flowfield structure for the 3-D swept compression corner at Mach 3 for $(\alpha, \lambda) = (24, 40)$ deg was determined, including a detailed quantitative description of the surfaces of separation and attachment.

* References are included in Section V.

** Fiscal Years (FY) refer to the Federal fiscal year (i.e., October to September).

3. Investigate Methods for Control and Modification of 3-D Turbulent Interaction Flowfields

The understanding of the flowfield structure of 3-D turbulent interactions provides the opportunity for investigation of methods for control and modification of the interaction flowfields. During FY87 a significant effort was focused on determining the effect of surface bleed on the flowfield structure of the 3-D sharp fin interaction.

4. Develop a Unified Understanding of the Flowfield Structure of 3-D Turbulent Interactions

A fourth objective is the understanding of the flowfield structure within broad families of 3-D turbulent interactions. The research effort to date has focused on the family of dimensionless 3-D shock generators (e.g., 3-D sharp fin and 3-D swept compression corner). The results have shown that the flowfield structure is similar for both configurations, namely, a large vortical structure. Further research is in progress to determine the universality of this structure to other configurations.

The research program has achieved significant progress towards these objectives. The present report details the progress during FY87 (1 October 1986 - 30 September 1987), and describes the research program for FY88 (1 October 1987 - 30 September 1988).

Section II. Research Accomplishments for FY87 and Research Program for FY88

A. Research Accomplishments for FY87 (1 October 1986 - 30 September 1987)

The research program has followed the basic tasks outlined in the original proposal submitted to Dr. James Wilson on 4 April 1986. Four specific research tasks were outlined for FY87, namely, i) the development and validation of theoretical models for 3-D shock wave-turbulent boundary layer interaction, ii) the determination of the flowfield structure of 3-D turbulent interactions for selected geometries, iii) the investigation of the control and modification of 3-D turbulent interactions, and iv) the development of a unified understanding of the flowfield structure of 3-D turbulent interactions. The progress during FY87 in these four areas is summarized in this section. Complete details of the research activity are provided in the papers presented at the AIAA 26th Aerospace Sciences Meeting (see Section VI).

The overall research program is closely coordinated with the computational research of Dr. C. C. Horstman (NASA Ames Research Center) and the experimental research of Prof. S. Bogdonoff (Princeton University). Drs. Knight, Horstman and Prof. Bogdonoff meet frequently to select specific 3-D shock wave-turbulent boundary layer interactions for detailed study. Separate, independent computations are then performed for the configuration by Drs. Knight and Horstman, and the calculated flowfields are compared with the experimental measurements of Bogdonoff. This close collaboration between theory and experiment is a critical element of the success of the program.

Research Task No. 1 : Develop and Validate Theoretical Models for 3-D Shock Wave-Turbulent Boundary Layer Interactions

The theoretical model is the 3-D Reynolds-averaged compressible Navier-Stokes equations, combined with a model for the Reynolds stresses and turbulent heat flux. The Reynolds stresses are modelled using a turbulent eddy viscosity; the turbulent heat flux is obtained from the turbulent Reynolds stresses assuming a constant turbulent Prandtl number equal to 0.9. Three separate turbulent eddy viscosity models are employed, namely, i) the algebraic model of Baldwin and Lomax, ii) the algebraic model of Cebeci and Smith, and iii) the k- ϵ model of Jones and Launder. The computations are performed by the principal investigator (using the Baldwin-Lomax model) and Dr. C. C. Horstman (using the Cebeci-Smith and k- ϵ models) employing the CYBER 205 and CRAY-X/MP, respectively.

The theoretical models have been successfully applied to the prediction of the 3-D sharp fin interaction (Knight *et al* 1987a). During FY86 the model was successfully applied to the 3-D swept compression corner for $(\alpha, \lambda) = (24, 60)$ deg at $Re_{\delta_{\infty}} = 1.4 \times 10^5$ and 9×10^5 (Knight *et al* 1987b). The computed flowfields using the two turbulence models were compared with the experimental data from the Princeton Gas Dynamics Laboratory for surface pressure, and boundary layer profiles of pitot pressure and yaw angle. For the lower Reynolds number cases, the computed surface pressure displayed significant disagreement with experiment,

although specific features (e.g., upstream influence location, peak corner pressure) were accurately predicted. The reason for the disagreement is not clear, and is the subject of current study. For the high Reynolds number case, the computed flowfields showed good agreement with experimental measurements of surface pressure, and boundary layer profiles of pitot pressure and yaw angle (Knight *et al* 1987b).

During FY87 the theoretical models were applied to the 3-D swept compression corner for a different sweep angle, specifically, the $(\alpha, \lambda) = (24, 40)$ deg configuration, at $Re_{\delta_{\infty}} = 2.6 \times 10^5$ and 8.1×10^5 . Computations were performed by Knight using the Baldwin-Lomax model. Calculations were performed earlier by Horstman using the Jones-Launder ($k-\epsilon$) and Cebeci-Smith turbulence models. The computed flowfields were compared with the experimental data of Settles and McKenzie (Settles *et al* 1986) and Ketchum and Bogdonoff (Knight *et al* 1988). The experimental data include surface pressure and boundary layer profiles of pitot pressure and yaw angle. A detailed comparison of theory and experiment is presented in Knight *et al* (1988)*. The results of the comparison may be summarized as follows :

1. Surface Pressure

The calculated surface pressure obtained using the Baldwin-Lomax model underpredicts the position of upstream influence (i.e., the location of the initial pressure rise). The predictions using the Cebeci-Smith and Jones-Launder models are in closer agreement with experiment; however, additional grid refinement studies are needed to determine the effect of grid resolution for the computations using the Cebeci-Smith and Jones-Launder models. The Baldwin-Lomax model provides an accurate prediction of the plateau pressure in the vicinity of the corner line, while the Cebeci-Smith and Jones-Launder models overpredict the plateau pressure.

2. Pitot Pressure and Yaw Angle

The computed pitot pressure and yaw angle profiles are observed to be remarkably insensitive to the turbulence model, and in good agreement with experimental measurements. The computed yaw angles in the immediate vicinity of the surface (i.e., the lower 10% of the boundary layer) are observed to be sensitive to the turbulence model, and differences of 10% - 15% are observed.

3. Surface Visualization

The computed surface skin friction lines exhibit qualitative agreement with the experimental kerosene-lampblack surface visualization. The calculated line of coalescence occurs downstream of the experimental position, with a typical angular difference of approximately 10%. The line of divergence is evident on the compression ramp surface in both the computation and experiment.

* Included in Section VI.

**Research Task No. 2: Determination of Physical Structure
 of 3-D Turbulent Interactions for Specific Geometries**

The research program has focused on the development of flowfield models for 3-D turbulent interactions. This effort is divided into two major categories, namely, 1) the development of sophisticated flowfield analysis and visualization tools, and 2) the determination of flowfield models using graphical techniques. These efforts are described below.

Development of Sophisticated Flowfield Analysis and Visualization Tools

During FY86 a major new facility was established in the College of Engineering to facilitate large scale scientific computation. This facility includes a Convex C-1 minisupercomputer, two Sun 3/180 file servers with 1.5 GByte disk storage, nine Sun graphics workstations (including two color workstations), and a variety of hardcopy devices (color thermal hardcopy and laser printers (4)). This facility was developed with funds received from i) the State of New Jersey's Commission on Science and Technology, and ii) Rutgers University. Additional support has been received from the Air Force Office of Scientific Research. The current Director of the facility is Prof. Abdel Zebib, Department of Mechanical and Aerospace Engineering, who succeeded Prof. Doyle Knight on 1 October 1987.

A significant effort has focused on development of software tools for the visualization of streamlines in order to ascertain the flowfield structure. The following tasks have been accomplished during FY87 :

1. Development of a general particle tracing code

A generalized three dimensional particle tracing computer code was completed FY87. The program permits a variety of user-specified interpolation schemes (linear and quadratic) to integrate the motion of a fluid particle within an arbitrary grid system. A complete description of the algorithm is provided in Raufer (1987). The program was successfully tested against a previous code, modelled after the particle tracing algorithm of Pieter Buning, NASA Ames Research Center (Buning 1984). The code has been extensively utilized in determining the flowfield structure of the 3-D swept compression corner (see below).

2. Development of graphics software for visualization of particle traces

A sophisticated, menu-driven graphics software program for the Sun workstations was completed in FY87. The program, written by Dr. Sandy Walther (Consultant), provides a convenient interface for examining particle pathlines. The tiled menus permit rapid selection of user-specified visualization parameters (e.g., location of the eye of the observer, picture plane, etc.).

3. Development of Analysis Code for Determining Viscous and Inviscid Effects

A research effort was initiated in FY87 to develop a computer code to examine the contributions to the rate of change of the mean kinetic energy ("mechanical energy") along a flow streamline. The mechanical energy equation is

$$D(\frac{1}{2}u_i u_i)/Dt = -(u_i/\rho)\partial p/\partial x_i + (u_i/\rho)\partial \tau_{ij}/\partial x_j$$

where $\frac{1}{2}u_i u_i$ is the mean kinetic energy per unit mass, $D/Dt = \partial/\partial t + u_j \partial/\partial x_j$, (u_1, u_2, u_3) is the cartesian velocity vector, (x_1, x_2, x_3) are the cartesian coordinates, p is the static pressure, ρ is the density, τ_{ij} is the total (viscous plus turbulent) stress tensor, and the Einstein summation convention is employed. There are two contributions to the rate of change of the mean kinetic energy per unit mass. The first term, $-(u_i/\rho)\partial p/\partial x_i$, is an inviscid effect associated with compression or dilation. The second term, $(u_i/\rho)\partial \tau_{ij}/\partial x_j$, represents the effect of the viscous and turbulent stresses. A series of flow streamlines are generated by integrating the motion of a fluid particle, released at a selected upstream position, through the computed flowfield. The mean kinetic energy equation is integrated simultaneously along the streamline, i.e.,

$$\frac{1}{2}u_i u_i = \frac{1}{2}u_i u_i|_0 + \int \{-(u_i/\rho)\partial p/\partial x_i + (u_i/\rho)\partial \tau_{ij}/\partial x_j\} ds/V$$

where $\frac{1}{2}u_i u_i|_0$ is the initial mean kinetic energy at the point of release of the fluid particle, ds is the infinitesimal arclength along the streamline and $V = \sqrt{u_i u_i}$. The separate contributions of the integrands $-(u_i/\rho)\partial p/\partial x_i$ and $(u_i/\rho)\partial \tau_{ij}/\partial x_j$ provide a quantitative measure of the inviscid and viscous contributions to the rate of change of the mean kinetic energy.

Determination of Flowfield Models

During the past year, a significant effort was focused on the determination of the flowfield structure for the 3-D swept compression using the computed flowfields obtained with the Baldwin-Lomax turbulence model. These flowfields had been validated by comparison with the experimental data of Ketchum and Bogdonoff (Knight *et al* 1988), Settles and McKenzie (Settles *et al* 1986), Settles and Teng (Settles and Teng 1984), and Ruderich and Mao (Knight *et al* 1987b). Details of the validation are presented in Knight *et al* (1987b) and Knight *et al* (1988). The flowfield analysis was performed using the software and graphical techniques described above. Efforts were focused on the 3-D swept compression corner for the $(\alpha, \lambda) = (24, 40)$ and $(24, 60)$ deg configurations at Mach 3 for $Re_{\delta_{\infty}} = 1.4 \times 10^5$ to 9×10^5 . The principal conclusions, described in detail in Knight *et al* (1988), are the following :

1. Vortical Structure

The 3-D swept compression corner flowfield is dominated by a large vortical structure for both the $(\alpha, \lambda) = (24, 40)$ and $(24, 60)$ deg configurations at Mach 3. The overall structure is characterized by two surfaces (Fig. 3), namely, 1) the surface emanating from the line of separation or coalescence (denoted as 'Surface No. 1'), and 2) the surface intersecting the line of attachment or divergence (denoted as 'Surface No. 2'). The fluid contained between the wall and the second surface is entrained within the vortex, while the fluid above the second surface passes over the vortex and moves up the ramp.

2. Viscous and Inviscid Effects

The contributions to the rate of change of the mean kinetic energy were evaluated for a series of streamlines for the $(\alpha, \lambda) = (24, 40)$ deg configuration at $Re_{\delta_{\infty}} = 8.1 \times 10^5$. A

detailed description of this analysis is presented in Knight *et al* (1988). It was observed that the rate of change of the mean kinetic energy was principally due to *inviscid* effects except for streamlines originating very close to the surface in the upstream boundary layer (i.e., $y < 0.05\delta_\infty$). A similar analysis is in progress for the $(\alpha, \lambda) = (24, 40)$ deg configuration for $Re_{\delta_\infty} = 2.6 \times 10^5$ and the $(\alpha, \lambda) = (24, 60)$ deg configuration at $Re_{\delta_\infty} = 1.4 \times 10^5$ and 9×10^5 .

These results are consistent with the previous observation regarding the insensitivity of the computed pitot pressure and yaw angle profiles to the turbulence model employed, except in the immediate vicinity of the surface. The 3-D turbulent interactions investigated are therefore principally rotational and inviscid within the boundary layer, except close to the wall.

Research Task No. 3: Investigate Methods for Control and Modification of 3-D Turbulent Interactions

The principal function of a conventional high speed aircraft inlet is to provide uniform, high total pressure, subsonic flow at the compressor face. It has long been observed that boundary layer separation within the inlet can lead to regions of low total pressure recovery at the inlet surface, and subsequent degradation of engine performance. Boundary layer bleed has traditionally been employed in high speed aircraft inlets to prevent boundary layer separation.

The development of accurate theoretical models for the 3-D sharp fin and swept compression corner configurations provides the opportunity for investigation of methods to control and modify these interactions. During FY87 efforts have focused on the 3-D sharp fin configuration and modification by surface bleed.

The focus of the activity on modification by surface bleed is the 3-D sharp fin interaction. This configuration is analogous to the sidewall interaction in a high speed inlet, with the sharp fin representing the ramp surface, and the flat plate representing the inlet sidewall. It is known that the effect of the sidewall interaction is to generate substantial spanwise flow which, upon interaction with the cowl (opposite the ramp), causes substantial low speed flow within the cowl boundary layer and subsequent low pressure recovery at the compressor face. The objective of this research activity, therefore, is to determine the effect of surface bleed on the flat plate (inlet sidewall) on the large vortical structure.

A series of computations have been performed for the 3-D sharp fin at Mach 3 for a fin angle of 20 deg at $Re_{\delta_\infty} = 9 \times 10^5$. Boundary layer bleed was provided in a triangular region between the line of upstream influence (as defined by the surface pressure) and the theoretical inviscid shock location. Three separate bleed flow rates (1%, 2.5% and 5% based on $\rho_\infty U_\infty$) were employed. These represent moderate to high bleed flow rates on basis of current design practice.

A detailed description of the results is provided in Gaitonde and Knight (1988)*. The principal conclusions are :

* Included in Section VI

1. Effect on Vortical Structure

The bleed has a negligible effect on the vortical structure. The large vortex, representing the principal structure of the 3-D turbulent interaction, is essentially unaffected in size and strength. This represents a significant, and indeed surprising, result. In particular, it brings into question the efficacy of boundary layer bleed for sidewall interactions in high speed inlets.

2. Effect on Compression Wave Ahead of Shock

The compression wave system, located upstream of the shock, is tightened by the surface bleed, which effectively reduces the displacement thickness of the interaction. The reduction in size of the compression region is evident in the pitot pressure and static pressure profiles.

3. Effect on Surface Skin Friction Lines

The line of coalescence is observed to move towards the downstream boundary of the bleed region. The surface skin friction lines between the lines of coalescence and divergence show the same qualitative behavior as observed for the no bleed case.

**Research Task No. 4: Develop a Unified Understanding of the
Flowfield Structure of 3-D Turbulent Interactions**

On the basis of detailed examination of particle traces for the 3-D swept compression corner at $(\alpha, \lambda) = (24, 40)$ and $(24, 60)$ deg during the present year, it is evident that the flowfield structure for these 3-D swept compression corner configurations and the 3-D sharp fin are qualitatively identical. This represents the first step in development of a more unified theory of flowfield structures for 3-D turbulent interactions.

B. Research Program for FY88 (1 October 1987 - 30 September 1988)

The research program for FY88 is characterized by two major themes, namely, i) the continuation of the research effort in supersonic shock wave-turbulent boundary layer interaction, and ii) the initiation of a significant research activity in 3-D hypersonic shock wave-turbulent boundary layer interaction. The basic four objectives, outlined in the original proposal (Knight 1986b) and described in Section I, are pertinent to both the supersonic and hypersonic research activity. The research tasks for the remainder of FY88 are described below in terms of the four objectives. It is noted that some of the activities are expected to continue into FY89.

**Research Task No. 1 : Develop and Validate Theoretical Models
for 3-D Shock Wave-Turbulent Boundary Layer Interactions**

The recent establishment of the National Aerospace Plane project (NASP) has led to

renewed interest in hypersonic flight. The phenomena of three dimensional shock wave-turbulent boundary layer interaction is prevalent in hypersonic flight, occurring in a variety of practical vehicle configurations. Despite an active research effort in hypersonic flows in the late sixties and early seventies, a complete understanding of 3-D hypersonic turbulent interactions has not been achieved (Holden 1986). Recently, Horstman (1987a) has studied 2-D hypersonic turbulent boundary layer interactions using the k- ϵ turbulence model and three different modifications to account for hypersonic compressibility effects. He concluded that no single turbulence model is capable of accurate prediction of the experimental data. The applicability of this result to 3-D hypersonic turbulent interactions, however, is not clear. Recent experimental and theoretical results at Mach 3 have shown that simple turbulence models (i.e., zero equation and two equation eddy viscosity models) are capable of accurate simulation of a variety of 3-D turbulent interactions (Knight *et al* 1987a, Knight *et al* 1987b, Knight *et al* 1988), while failing to accurately reproduce the limiting 2-D turbulent interaction (Ong and Knight, 1986). The success in 3-D supersonic turbulent interactions was attributed to the nature of the interaction, specifically, the flowfields investigated were observed to be essentially inviscid and rotational, except in a small fraction of the turbulent boundary layer adjacent to the surface where the effects of turbulence were observed to be significant. A collaborative experimental and theoretical investigation of 3-D hypersonic turbulent interactions is therefore required.

The proposed research project involves the numerical simulation of the 3-D hypersonic turbulent interaction generated by a sharp fin. The flow configuration is shown in Fig. 1. An equilibrium turbulent boundary layer develops on the flat plate. The deflection of the fin creates an oblique shock wave, which interacts with the turbulent boundary layer on the flat plate. The selection of this configuration was motivated by several factors. First, the recent collaborative experimental and theoretical effort involving the principal investigator, NASA Ames Research Center and Princeton Gas Dynamics Laboratory (Knight *et al* 1987a) has developed a detailed understanding of the flowfield structure of the 3-D sharp fin turbulent interaction at Mach 3. Second, a series of 3-D sharp fin experiments are planned at hypersonic speeds (Mach 7 and 10) at NASA Ames Research Center in FY88 and FY89 (Horstman 1987b).

A series of computations will be performed for the 3-D sharp fin configuration at Mach 7 at fixed Reynolds number for several fin angles α . Additional computations may be performed at Mach 10. The flow conditions will be selected to agree with the planned experiments at NASA Ames. Although the precise requirements for the number of grid points and cpu time depends on the specific case, experience has indicated that typically 100,000 grid points and 10 CYBER 205 cpu hrs are required (Knight *et al* 1987b) for each case.

The computed results will be compared with the experimental data. Present plans include measurements of surface pressure and heat transfer, surface oil film visualization, and boundary layer profiles of pitot and static pressure, velocity, and turbulence fluctuations. The data and graphics postprocessing will be performed at the Rutgers College of Engineering Supercomputer Remote Access and Graphics Facility.

**Research Task No. 2: Determination of Physical Structure
of 3-D Turbulent Interactions for Specific Geometries**

Recent collaborative efforts involving the principal investigator, NASA Ames Research Center and the Princeton Gas Dynamics Laboratory have focused on the understanding of the flowfield structure for two specific dimensionless configurations, namely, the sharp fin (Fig. 1) and the swept compression corner (Fig. 2). On the basis of these investigations, conducted at Mach 3 over a Reynolds number range from 2.3×10^5 to 9×10^5 , a view of the overall flowfield structure has emerged. The flowfield is inviscid and rotational over a majority of the interaction domain, except within a narrow region adjacent to the surface where the effects of turbulent mixing are significant. For both the sharp fin at Mach 3 (and α up to 20 deg) and the swept compression corner at Mach 3 (and $(\alpha, \lambda) = (24, 40)$ and $(24, 60)$ deg), the flowfield is dominated by a large vortical structure.

A series of experiments were performed recently at the Princeton Gas Dynamics Laboratory to investigate the effect of the shock generating geometry on the interaction (Kimmel 1987). Three configurations were selected, namely, the sharp fin (Fig. 1), swept compression corner (Fig. 2), and semicone (Fig. 4). The geometrical characteristics were selected to obtain similar shock strengths. Specifically, the sharp fin angle $\alpha = 17.5$ deg, the angle of compression and sweep for the swept compression corner are $\alpha = 30$ deg and $\lambda = 60$ deg, and the semicone half angle $\gamma = 25$ deg respectively. Each configuration was examined at Reynolds numbers of 1.6×10^5 and 9.1×10^5 . For the lower Reynolds number, detailed surface pressure and kerosene-lampblack flow visualization was performed. At the higher Reynolds number, experimental data include both surface pressure and kerosene-lampblack flow visualization, and boundary layer profiles of pitot pressure, static pressure, and yaw angle.

The three configurations exhibited conical similarity, with the flow surface and flowfield variables exhibiting two distinct regions. The first region, extending from upstream to a point downstream of the shock system, displayed a 'quasi-conical free interaction'. In this region, for example, the experimental pressure distribution, displayed along a line normal to the inviscid shock, was virtually identical for the three configurations *despite their significant geometrical differences*. A second region, downstream of the first region and denoted the 'model dominated region', showed no similarity of profiles.

The explanation for the quasi-conical free interaction is not clear. It is anticipated that all three flowfields display a large vortical structure. The sharp fin at $\alpha = 17.5$ deg is intermediate to a series of computed flows ($\alpha = 10$ and 20 deg) which have displayed a large vortical structure (Knight *et al* 1987a). The swept compression corner at $(\alpha, \lambda) = (30, 60)$ deg is close to the previous computation of Knight *et al* at $(\alpha, \lambda) = (24, 60)$ deg. The semicone, however, has not been computed previously. It is unclear, however, why this vortical structure should yield nearly identical pressure distributions in the quasi-conical free interaction region.

The proposed research will focus on the three configurations, namely, the sharp fin at $\alpha = 17.5$ deg, the semicone at $\gamma = 25$ deg, and the swept compression corner at $(\alpha, \lambda) = (30, 60)$ deg. Computations will be performed at Mach 3 for Reynolds numbers of 1.6×10^5 and 9.1×10^5 . Although the precise requirements for the number of grid points and cpu time depends on the specific case, experience has indicated that typically 100,000 grid points and 10 CYBER 205 cpu hrs are required (Knight *et al* 1987b) for each case.

The computed results will be compared with the experimental data of Kimmel (1987).

The computed flowfields will be analyzed to determine the flowfield structure, and examine the reasons for the quasi-conical similarity. The data and graphics postprocessing will be performed at the Rutgers College of Engineering Supercomputer Remote Access and Graphics Facility.

Research Task No. 3: Investigate Methods for Control and Modification of 3-D Turbulent Interactions

The research activity on control and modification of 3-D turbulent interactions is continued in FY88. Two specific activities are in progress :

1. 3-D Sharp Fin in the Presence of Bleed

The research effort on the effects of boundary layer bleed for the 3-D sharp fin configuration focused on a specific bleed configuration in FY87, namely, a triangular bleed region confined between the line of upstream influence and the inviscid shock (Section II.A). A series of computations were performed at Mach 3 for a fin angle of 20 deg at $Re_{\delta_{\infty}} = 9 \times 10^5$. During the present year, the same configuration will be examined with a different bleed schedule, namely, a bleed region confined between the inviscid shock and the fin surface. These two configurations will therefore provide an examination of the effects of bleed throughout the entire interaction region.

2. 3-D Intersecting Shock Wave-Turbulent Boundary Layer Interaction

A novel concept was proposed by Mee and Stalker (1987) to control 3-D shock wave-turbulent boundary layer interactions. They argued that "intersecting shock interactions can produce a given overall pressure rise with less likelihood of separation than an equivalent strength single shock interaction". A model of the flow is displayed in Fig. 5. Two sharp fins, mounted normal to the flat plate, generate oblique shock waves which intersect. The fin angles may be equal or dissimilar, yielding a symmetric or asymmetric interaction, respective. The initial 3-D shock wave-turbulent boundary layer interaction associated with each oblique shock generates a vortical structure whose strength is dependent on the flow conditions and fin angle (i.e., initial pressure rise). The sense of rotation of the flow within the vortical structures are of opposite sign.

The concept of Mee and Stalker is unproven, however, and additional computational and experimental research is required to determine its validity. In FY 88, two specific computations are planned. First, a calculation will be performed* for the strongest symmetric intersecting shock configuration of Mee and Stalker. This case corresponds to an incoming Mach number of 1.85, Reynolds number $Re_{\delta_{\infty}} = 7.8 \times 10^4$, and symmetric sharp fins with an angle of 5 deg. This represents a rather weak interaction, with an overall pressure rise across the intersection shocks $p_{\text{final}}/p_{\text{upstream}}$ equal to 1.7. Second, a series of computations will be performed for the intersecting shock configurations currently under study at the Princeton Gas Dynamics Laboratory. These cases correspond to an incoming Mach number of 1.85, Reynolds number $Re_{\delta_{\infty}} = 1 \times 10^5$ to 2×10^5 , and symmetric sharp fins with angles of 4, 6 and 8 deg. The experimental program at the Princeton Gas Dynamics Laboratory includes measurements of surface pressure and surface flow visualization. These configurations represent significantly stronger interactions, with overall pressure rises $p_{\text{final}}/p_{\text{upstream}} = 1.8, 2.4, 3.1$ for fin angles of 4, 6, and 8 deg.

* This computation has been completed, and is included in the paper by Gaitonde and Knight in Section VI.

**Research Task No. 4: Develop a Unified Understanding of the
Flowfield Structure of 3-D Turbulent Interactions**

The research program continues to focus on the objective of developing a unified understanding of the flowfield structure of 3-D turbulent interactions. In the previous year, it was observed that the flowfield structure for specific configurations of the 3-D sharp fin and 3-D swept compression corner interactions was similar (i.e., a large vortical structure). Efforts continue to identify similarities in the different configurations examined under the previous three objectives.

Section III. Publications and Scientific Interactions

A. Written Publications - Cumulative Chronological List

1. 1 October 1981 - 30 September 1982

- a. Knight, D., "Application of Curvilinear Coordinate Generation Techniques to the Computation of Internal Flows", in *Numerical Grid Generation - Proceedings of a Symposium on the Numerical Generation of Curvilinear Coordinates and their Use in the Numerical Solution of Partial Differential Equations*, North-Holland, New York, 1982, pp. 357-384.***
- b. Knight, D., "A Hybrid Explicit-Implicit Numerical Algorithm for the Three-Dimensional Compressible Navier-Stokes Equations", AIAA Paper No. 83-0223, AIAA 21st Aerospace Sciences Meeting, January 10-13, 1983. Published in *AIAA J.*, Vol. 22, Aug 1984, pp. 1056-1063.***
- c. Visbal, M., and Knight, D., "Generation of Orthogonal and Nearly Orthogonal Coordinates with Grid Control Near Boundaries", *AIAA J.*, Vol. 20, No. 3, March 1982, pp. 305-206.*****

2. 1 October 1982 - 30 September 1983

- a. Knight, D., "Calculation of a Simulated 3-D High Speed Inlet Using the Navier-Stokes Equations", AIAA Paper No. 83-1165, AIAA/SAE/ASME 19th Joint Propulsion Conference, Seattle, Washington, June 27-29, 1983.
- b. Visbal, M., and Knight, D., "Evaluation of the Baldwin-Lomax Turbulence Model for Two-Dimensional Shock Wave Boundary Layer Interactions", AIAA Paper No. 83-1697, AIAA 16th Fluid and Plasma Dynamics Conference, Danvers, Mass., July 12-14, 1983. Published in the *AIAA J.*, Vol. 22, July 1984, pp. 921-928.*

3. 1 October 1983 - 30 September 1984

- a. Knight, D., "Numerical Simulation of Three-Dimensional Shock- Turbulent Boundary Layer Interaction Generated by a Sharp Fin", AIAA Paper No. 84-1559, AIAA 17th Fluid Dynamics, Plasmadynamics and Lasers Conference, June 25-27, 1984. Published in the *AIAA J.*, Vol. 23, December 1985, pp. 1885-1891.*

* Research sponsored by AFOSR Grant 82-0040

** Research sponsored by AFOSR Grant 80-0072

*** Research sponsored by AF Contract F-33615-C-3008

- b. York, B., and Knight, D., "Calculation of Two-Dimensional Turbulent Boundary Layers Using the Baldwin-Lomax Model", AIAA 23rd Aerospace Sciences Meeting, Jan 14-17, 1984. Published in the *AIAA J.*, Vol. 23, Dec 1985, pp. 1849-1850.
- 4. 1 October 1984 - 30 September 1985
 - a. Knight, D., "Modelling of Three Dimensional Shock Wave Turbulent Boundary Layer Interactions", in *Macroscopic Modelling of Turbulent Flows*, Lecture Notes in Physics, Vol. 230, Springer-Verlag, NY, 1985, pp. 177-201.
 - b. Knight, D., Horstman, C., Shapey, B., and Bogdonoff, S., "The Flowfield Structure of the 3-D Shock Wave - Boundary Layer Interaction Generated by a 20 deg Sharp Fin at Mach 3", AIAA Paper No. 86-0343, AIAA 24th Aerospace Sciences Meeting, January 6-9, 1986. Accepted for publication in the *AIAA J.*, to appear 1987.
 - c. Ong, C., and Knight, D., "A Comparative Study of the Hybrid MacCormack and Implicit Beam-Warming Algorithms for a Two-Dimensional Supersonic Compression Corner", AIAA Paper No. 86-0204, AIAA 24th Aerospace Sciences Meeting, January 6-9, 1986. Accepted for publication in the *AIAA J.*, to appear March 1987.
- 5. 1 October 1985 - 30 September 1986
 - a. Knight, D., Horstman, C., Ruderich, R., Mao, M.-F., and Bogdonoff, S., "Supersonic Flow Past a 3-D Swept Compression Corner at Mach 3", AIAA Paper No. 87-0551, AIAA 25th Aerospace Sciences Meeting, January 12-15, 1987.
- 6. 1 October 1986 - 30 September 1987
 - a. Knight, D., Rauffer, D., Horstman, C., Ketchum, A., and Bogdonoff, S., "Supersonic Turbulent Flow Past a Swept Compression Corner at Mach 3 : Part II", AIAA Paper No. 88-0310, AIAA 26th Aerospace Sciences Meeting, January 11-14, 1988.
 - b. Gaitonde, D., and Knight, D., "Numerical Experiments on the 3-D Shock Wave-Boundary Layer Interaction Generated by a Sharp Fin", AIAA Paper No. 88-0310, AIAA 26th Aerospace Sciences Meeting, January 11-14, 1988.

B. Visitors to Rutgers University : 1 October 1986 - 30 September 1987

The following individuals visited the principal investigator to discuss elements of the research program :

- 1. Dr. C. C. Horstman, NASA Ames Research Center, 15-16 October 1986.

2. Dr. Russel Calfrisch, New York University, 9 December 1986.
3. Dr. C. C. Horstman, NASA Ames Research Center, 2 April 1987.
4. Dr. Peter Eiseman, Columbia University, 24 April 1987.
5. Dr. Chin-Shin Lin, NASA Lewis Research Center, 27 April 1987.

**C. Spoken Papers Presented at Technical Meetings :
1 October 1986 - 30 September 1987**

1. Knight, D., Horstman, C., Sapey, B., and Bogdonoff, S., "Three Dimensional Shock Wave-Turbulent Boundary Layer Interaction Generated by a Swept Compression Corner", Thirty-Ninth Annual Meeting, Division of Fluid Dynamics, American Physical Society, November 23-25, 1986, *Bulletin of the American Physical Society*, Vol. 31, No. 10, November 1986, p. 1693.
2. Knight, D., Horstman, C., Ruderich, R., Mao, M.-F., and Bogdonoff, S. 1987b Supersonic Turbulent Flow Past a 3-D Swept Compression Corner at Mach 3. AIAA Paper No. 87-0551. AIAA 25th Aerospace Sciences Meeting, January 12-15, 1987, Reno, NV.

D. Seminars : 1 October 1986 - 30 September 1987

1. Knight, D., "Theoretical Investigation of 3-D Shock Wave - Turbulent Boundary Layer Interactions", United Technologies Research Center, Hartford, CT, 9 April 1987.
2. Knight, D., "Numerical Simulation of 3-D Shock Wave - Turbulent Boundary Layer Interaction Generated by a Swept Compression Corner", Argonne National Laboratory, Batavia, IL, 11 June 1987.

Section IV. List of Personnel and Degrees Awarded

A. Personnel : 1 October 1986 - 30 September 1987

Principal Investigator :

Prof. Doyle Knight
Department of Mechanical and Aerospace Engineering

Graduate Research Assistants working on this project :

Supported by AFOSR Grant 86-0266 :

Ms. Denise Raufer
Department of Mechanical and Aerospace Engineering

Supported by Other Sources :

Mr. Datta Gaitonde
Department of Mechanical and Aerospace Engineering
Grant : New Jersey Commission on Science and Technology

Mr. Yan Zang
Department of Mechanical and Aerospace Engineering
Grant : Rutgers University Excellence Fellowship

B. Degrees Awarded : 1 October 1986 - 30 September 1987

Raufer, D., "The Development of a 3-D Particle Tracing Algorithm and Its Application to the Study of Swept Compression Corner Boundary Layer Interactions", MS Thesis, Department of Mechanical and Aerospace Engineering, October 1987.

Section V. References

- Baldwin, B., and Lomax, H. 1978 Thin Layer Approximation and Algebraic Model for Separated Turbulent Flows. AIAA Paper 78-257.
- Buning, P. 1984 Private Communication.
- Gaitonde, D., and Knight, D. 1988 Numerical Experiments on the 3-D Shock Wave - Boundary Layer Interaction Generated by a Sharp Fin. AIAA Paper No. 88-0309.
- Holden, M. 1986 A Review of Aerothermal Problems Associated with Hypersonic Flight. AIAA Paper No. 86-0267.
- Horstman, C., and Hung, C. 1979 Computation of Three-Dimensional Separated Flows at Supersonic Speeds. AIAA Paper No. 79-0002.
- Horstman, C. 1984 A Computational Study of Complex Three-Dimensional Compressible Turbulent Flow Fields. AIAA Paper No. 84-1556, AIAA 17th Fluid Dynamics, Plasma Dynamics and Lasers Conference.
- Horstman, C. 1987a Prediction of Hypersonic Shock-Wave/Turbulent Boundary Layer Interaction Flows. AIAA Paper NO. 87-1367.
- Horstman, C. 1987b Private Communication.
- Jones, W., and Launder, B. 1972 The Prediction of Laminarization with a Two-Equation Model of Turbulence. *Int. J. Heat and Mass Transfer*, Vol. 15, pp. 301-304.
- Kimmel, R. 1987 An Experimental Investigation of Quasi-Conical Shock Wave / Turbulent Boundary Layer Interactions. PhD Thesis, Department of Aerospace and Mechanical Engineering.
- Knight, D. 1984a A Hybrid Explicit-Implicit Numerical Algorithm for the Three-Dimensional Compressible Navier-Stokes Equations. *AIAA J.*, Vol. 22, pp. 1056-1061.
- Knight, D. 1984b Modelling of Three-Dimensional Shock Wave Turbulent Boundary Layer Interactions. Workshop on Macroscopic Modelling of Turbulent Flows and Fluid Mixtures. INRIA, Nice, France. December 1984. Also, *Lecture Notes in Physics*, Springer-Verlag, Vol. 230, 1985, pp. 177-201.
- Knight, D. 1984c Numerical Simulation of 3-D Shock Turbulent Boundary Layer Interaction Generated by a Sharp Fin. *AIAA J.*, Vol. 23, No. 12, December 1985, pp. 1885-1891.
- Knight, D. 1985 Theoretical Investigation of Three-Dimensional Shock Wave-Turbulent Boundary Layer Interactions. A Three Year Proposal for the Period Beginning 1 October 1985. Submitted to the Air Force Office of Scientific Research, 1 May 1985.
- Knight, D. 1986a Theoretical Investigation of Three-Dimensional Shock Wave-Turbulent Boundary Layer Interactions : Part IV. Interim Report for Period 1 October 1984 to 30 September 1985. Report RU-TR-163-MAE-F, Department of Mechanical and Aerospace Engineering, Rutgers University January 1986.
- Knight, D. 1986b Theoretical Investigation of Three-Dimensional Shock Wave-Turbulent Boundary Layer Interactions. A Three Year Proposal for the Period Beginning 1 October 1986. Submitted to the Air Force Office of Scientific Research, 4 April 1986.
- Knight, D., Horstman, C., Shapey, B., and Bogdonoff, S. 1987a Structure of the Supersonic Turbulent Flow Past a Sharp Fin. *AIAA J.*, Vol. 25, 1987, pp. 1331-1337.

- Knight, D., Horstman, C., Ruderich, R., Mao, M.-F., and Bogdonoff, S. 1987b Supersonic Turbulent Flow Past a 3-D Swept Compression Corner at Mach 3. AIAA Paper No. 87-0551. AIAA 25th Aerospace Sciences Meeting, January 12-15, 1987, Reno, NV.
- Knight, D., Raufer, D., Horstman, C., Ketchum, A., and Bogdonoff, S. 1988 Supersonic Turbulent Flow Past a Swept Compression Corner at Mach 3 : Part II. AIAA Paper 88-0310, AIAA 26th Aerospace Sciences Meeting, January 11-14, 1988, Reno, NV.
- Mee, D. 1986 Experiments Involving the Interactions of a Turbulent Boundary Layer with Single and Intersecting Fin-Induced Swept Shock Waves and Swept Expansion Fans. Technical Report 11/86, Dept. of Mech. Engr., University of Queensland, Australia.
- Mee, D., and Stalker, R. 1987 Investigation of Weak Shock-Shock and Shock-Expansion Intersection in the Presence of a Turbulent Boundary Layer. AIAA Paper 87-0549.
- Ong, C., and Knight, D. Hybrid MacCormack and Implicit Beam-Warming Algorithms for a Supersonic Compression Corner. *AIAA J.*, Vol. 25, 1987, pp. 401-407.
- Paynter, G. 1980 Analysis of Multiple Weak Glancing Shock Boundary Layer Interactions. AIAA Paper No. 80-0196.
- Raufer, D. 1987 The Development of a 3-D Particle Tracing Algorithm and Its Application to the Study of Swept Compression Corner Boundary Layer Interactions. MS Thesis, Department of Mechanical and Aerospace Engineering, Rutgers University, October 1987.
- Settles, G., and Teng, H. 1984 Cylindrical and Conical Upstream Influence Regimes of Three-Dimensional Shock/Turbulent Boundary Layer Interactions. *AIAA J.*, Vol. 22, 1984, pp. 194-200.
- Settles, G., Horstman, C., and McKenzie, T. 1986 "Experimental and Computational Study of a Swept Compression Corner Interaction Flowfield". *AIAA J.*, Vol. 24, pp. 742-752.

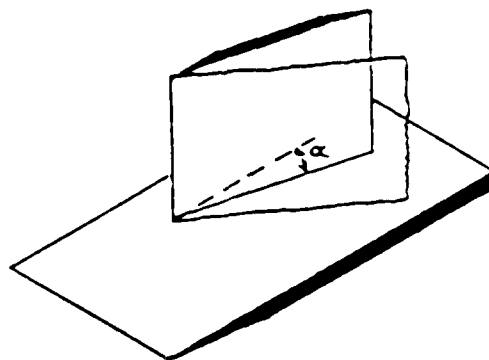


Fig. 1 3-D Sharp Fin

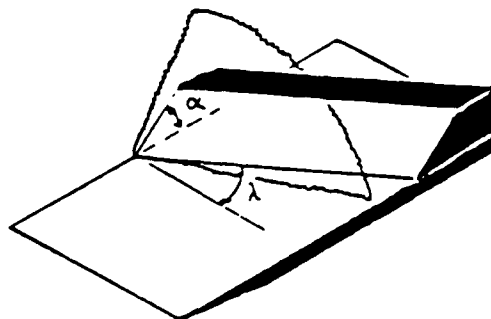


Fig. 2 3-D Swept Compression Corner

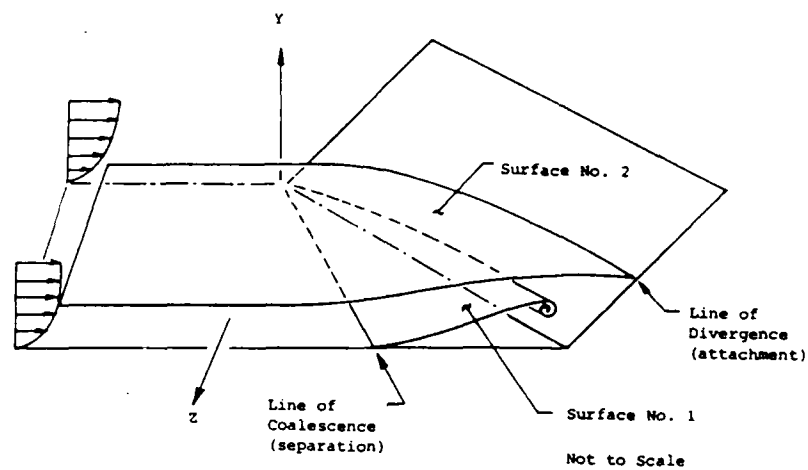


Fig. 3 Flowfield Structure of 3-D Swept Compression Corner

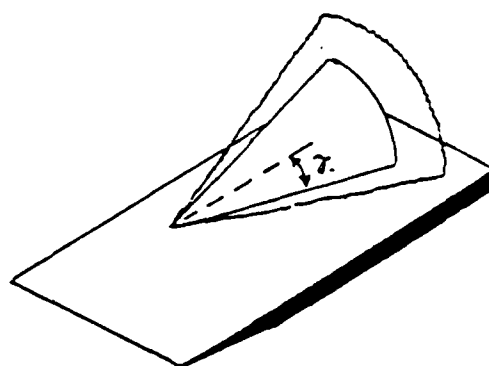


Fig. 4 3-D Semicone

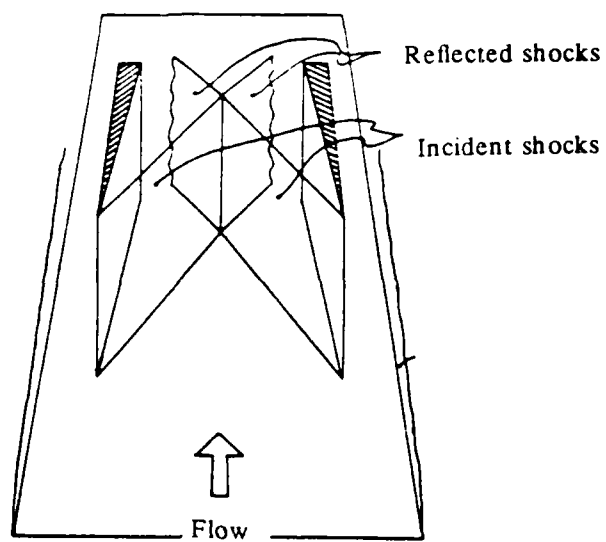


Fig. 5 3-D Intersecting Shock Waves

Section VI. Papers

"Supersonic Turbulent Flow Past a 3-D Swept Compression Corner at Mach 3 : Part II"

by D. Knight, D. Raufer, C. Horstman, A. Ketchum and S. Bogdonoff

AIAA Paper 88-0310

Presented at the AIAA 26th Aerospace Sciences Meeting
January 11-14, 1988
Reno, NV

*Supersonic Turbulent Flow
Past a Swept Compression Corner at Mach 3
Part II*

Doyle D. Knight* and Denise Raufert**
Department of Mechanical and Aerospace Engineering
Rutgers University
New Brunswick, NJ 08903

C. C. Horstman***
NASA Ames Research Center
Moffett Field, CA 94035

Andrew Ketchum**** and Seymour Bogdonoff*****
Department of Aerospace and Mechanical Engineering
Princeton University
Princeton, NJ 08540

Abstract

A combined experimental and theoretical investigation has continued for the 3-D shock wave-turbulent boundary layer interaction generated by a swept compression corner. The compression corner geometry is characterized by the angle of streamwise compression α and the angle of sweep λ . The present study focuses on the $(\alpha, \lambda) = (24, 40)$ deg configuration at $Re_{\delta_{\infty}} = 2.6 \times 10^5$ and 8.1×10^5 . Recent computations have been performed for this configuration using the Baldwin-Lomax algebraic turbulent eddy viscosity model. Previous computations were performed using the Cebeci-Smith algebraic turbulent eddy viscosity model and the Jones-Launder two-equation (k- ϵ) model. The results using these three models are compared in the present paper with the experimental measurements of Settles and McKenzie for $(\alpha, \lambda) = (24, 40)$ deg at $Re_{\delta_{\infty}} = 2.6 \times 10^5$ and 8.1×10^5 , and the experimental measurements of Ketchum and Bogdonoff at $Re_{\delta_{\infty}} = 8.1 \times 10^5$. The computed flowfields are generally in good agreement with experimental profiles of pitot pressure and

yaw angle at both Reynolds numbers, and are relatively insensitive to the turbulence model employed. The computed surface pressure underpredicts the upstream influence of the interaction. The flowfield, examined using particle tracing, manifests a large vortical structure. The quantitative details of the flowfield structure are examined for the $(\alpha, \lambda) = (24, 40)$ deg configuration, and compared to previous results for the $(\alpha, \lambda) = (24, 60)$ deg configuration. The rate of change of the mean kinetic energy along a streamline is investigated. The principal contribution is attributable to inviscid effects except for streamlines originating very close to the wall. This examination provides direct evidence that the flowfield structure is rotational and inviscid except in the immediate vicinity of the surface.

Introduction

The interaction between shock waves and turbulent boundary layers is an important problem in modern fluid mechanics, with applications to high speed aerodynamics and propulsion. The earliest observations were apparently made by Ferri^{1,2}, and the first systematic investigations were performed by Liepmann³ and Ackeret⁴. In a review of 3-D supersonic turbulent interactions in 1969, Greene remarked⁵,

"We have seen that present understanding of shock and boundary layer interactions in two-dimensional flow is not entirely satisfactory. In general three-dimensional flows it scarcely exists

* Professor; Associate Fellow, AIAA.

** Graduate Student; presently, Bell Laboratories.

*** Assistant Branch Chief; Associate Fellow, AIAA.

**** Graduate Student

***** Professor; Fellow, AIAA.

in any quantitative sense."

Within the past fifteen years, a significant effort has been focused on 3-D shock wave-turbulent boundary layer interactions (denoted "3-D turbulent interactions"). The research has employed experimental, computational, and analytical techniques. A general review of swept shock wave-turbulent boundary layer interactions has been presented by Settles and Dolling².

A series of collaborative experimental and theoretical investigations by the authors has focused on two specific dimensionless geometries for 3-D shock wave-turbulent boundary layer interactions, namely, the 3-D sharp fin (Fig. 1) and the 3-D swept compression corner (Fig. 2). The theoretical model is the Reynolds-averaged compressible Navier-Stokes equations, with turbulence incorporated using an turbulent eddy viscosity. Several different turbulent eddy viscosity models are employed, including the Baldwin-Lomax⁶ and Cebeci-Smith⁷ algebraic models and the Jones-Launder⁸ or k- ϵ two equation model. The governing equations are solved using two different numerical algorithms. The experiments utilize the high Reynolds number wind tunnel at the Princeton Gas Dynamics Laboratory. The 3-D sharp fin has been studied⁹⁻¹³ at Mach 3 for Reynolds numbers $Re_{\delta_{\infty}} = 2.5 \times 10^5$ to 9×10^5 and fin angle α up to 20 deg. It was observed that the computed results were in good agreement with the experimental data for surface pressure, and boundary layer profiles of pitot pressure, static pressure and yaw angle. The computed flowfields were found to be insensitive to the turbulence model employed, except in a small fraction of the boundary layer adjacent to the surface, where the computed profiles displayed modest differences amongst the predictions of the various turbulence models and the experiment. It was concluded, therefore, that the 3-D sharp fin interaction was principally inviscid and rotational, except in the aforementioned narrow region adjacent to the surface. The flowfield was observed to be dominated by a large vortical structure.

In a previous paper¹⁴, the 3-D swept compression corner for the $(\alpha, \lambda) = (24, 60)$ configuration was examined at $Re_{\delta_{\infty}} = 1.4 \times 10^5$ to 9×10^5 . Computations were performed using the Baldwin-Lomax and Jones-Launder turbulence models, and the results compared with

the experimental data of Ruderich, Mao and Bogdonoff. The computed flowfields for $Re_{\delta_{\infty}} = 9 \times 10^5$ were found to be in good agreement with the experimental data for surface pressure, and boundary layer profiles of pitot pressure and yaw angle. The computed surface pressure for the lower Reynolds number case, however, displayed significant (i.e., 25%) differences with experiment. The computed flowfields for the $Re_{\delta_{\infty}} = 9 \times 10^5$ case displayed a large vortical structure, with a topology similar to the 3-D sharp fin.

The present paper focuses on the 3-D swept compression corner for the $(\alpha, \lambda) = (24, 40)$ at $Re_{\delta_{\infty}} = 2.6 \times 10^5$ and 8.1×10^5 . Recent computations have been performed for this configuration using the Baldwin-Lomax model. Previous calculations were performed by Horstman¹⁵ using the Cebeci-Smith and Jones-Launder turbulence models. The objectives of the present effort are:

1. Accuracy of the theoretical models

The efficacy of the Baldwin-Lomax model for the $(\alpha, \lambda) = (24, 40)$ deg configuration is examined through comparison with the present experimental data of Ketchum and Bogdonoff and the prior experimental study of Settles *et al*¹⁵ for surface pressure, and boundary layer profiles of pitot pressure and yaw angle. These results are also compared with the previous computations of Horstman using the Cebeci-Smith and Jones-Launder models.

2. Determination of the Flowfield Structure

Provided reasonable agreement is obtained between the computed and measured data, the computed flowfields can be employed to ascertain the basic flowfield structure. The $(\alpha, \lambda) = (24, 40)$ deg configuration is examined, with emphasis on quantifying the nature of the topology of the flow. This includes the description of the distinct regions of the flowfield and an examination of the viscous and inviscid contributions to the rate of change of the mean kinetic energy.

Description of Experiments

The experiments were conducted in the high Reynolds number wind tunnel at the Princeton Gas Dynamics Laboratory. A description of the facility is provided in Vas and Bog-

donoff¹⁶. The facility is a blowdown tunnel with a 20 cm x 20 cm test section and a nominal Mach 3 test section. The total pressure for the $(\alpha, \lambda) = (24, 40)$ deg configuration was 683 kPa $\pm 1.8\%$ and 690 kPa $\pm 1.3\%$ for $Re_{\delta_{\infty}} = 2.6 \times 10^5$ and 8.1×10^5 , respectively. The total temperature for the $(\alpha, \lambda) = (24, 40)$ deg configuration was 265.4 deg K $\pm 1.6\%$ for both Reynolds numbers. The surface temperature was near adiabatic. The incoming boundary layer was an equilibrium, two-dimensional turbulent boundary layer which has been extensively surveyed^{16,17} and observed to satisfy the Law of the Wall and Wake^{18,19}. The nominal boundary layer thickness $\delta_{\infty} = 0.42$ cm and 1.27 cm for $Re_{\delta_{\infty}} = 2.6 \times 10^5$ and 8.1×10^5 , respectively. Detailed boundary layer profile measurements were performed for the $\delta_{\infty} = 1.27$ cm configuration. The size of the instrumentation limited the extent of the boundary layer profile data for the $\delta_{\infty} = 0.42$ cm case.

Description of Computations

A total of three different theoretical models are employed for the 3-D swept compression corner at $(\alpha, \lambda) = (24, 40)$ deg. The governing equations are the full mean three-dimensional compressible Navier-Stokes equations using mass-averaged variables²⁰ and strong conservation form²¹. Three separate turbulent eddy viscosity models are employed, namely, the algebraic models of Baldwin-Lomax⁶ and Cebeci-Smith⁷, and the two-equation (k- ϵ) model of Jones-Launder⁸. The molecular dynamic viscosity is specified by Sutherland's law. The molecular and turbulent Prandtl numbers are 0.73 and 0.9, respectively.

The computational domain is shown in Fig. 3. An equilibrium turbulent boundary layer profile is prescribed at the upstream boundary ABHG satisfying the measured momentum thickness. It is noted that the upstream boundary is parallel to the corner line, and hence swept downstream at an angle λ relative to the spanwise coordinate z . The calculations employing the Baldwin-Lomax model incorporated the variation in upstream boundary layer thickness on ABHG due to the sweep of ABHG. The calculations using the Cebeci-Smith and Jones-Launder models employed an average boundary layer profile. Previous computations at $(\alpha, \lambda) = (24, 60)$ deg have shown that the 3-D interaction is insensitive to moderate changes in the

upstream boundary layer thickness¹⁴. At the plane of symmetry AFEKLG, the normal component of the velocity is set to zero, and the normal gradient of the remaining flow variables is zero. On the solid surface ABCDEF, the velocity is zero, a fixed surface temperature (near adiabatic conditions) is prescribed, and the normal derivative of the static pressure is set to zero. At the right boundary BCDJIH, the gradient of the flow variables in a direction parallel to the corner line is set to zero. On the downstream boundary EDJK, the gradient of the flow variables is set to zero along a direction parallel to the x -axis and compression ramp surface. The upper boundary GHIJKL is fixed sufficiently far from the interaction that the flowfield is undisturbed and uniform freestream conditions are applied.

The computations using the Cebeci-Smith and Jones-Launder models were solved using the hybrid explicit-implicit algorithm of MacCormack²². The computations using the Baldwin-Lomax model were solved using the hybrid explicit-implicit algorithm of Knight¹⁰. Both algorithms have been highly vectorized for execution on CRAY and CYBER 205 computers, respectively.

The results of the three different theoretical models for the $(\alpha, \lambda) = (24, 40)$ deg compression corner at $Re_{\delta_{\infty}} = 2.6 \times 10^5$ are compared with the experimental data of Settles and McKenzie. The computations employing the Cebeci-Smith and Jones-Launder models utilized a grid of 27,200 points. The x -grid spacing was concentrated near the corner, with a minimum $\Delta x/\delta_{\infty} = 0.18$, and a maximum $\Delta x/\delta_{\infty} = 1.2$ at the upstream and downstream boundaries. The y -grid spacing was concentrated near the surface with the minimum $\Delta y/\delta_{\infty} = 2.78 \times 10^{-4}$, and the maximum $\Delta y/\delta_{\infty} = 1.39$ at the upper surface GHIJKL. The grid spacing adjacent to the surface satisfied $\Delta y u_w/v_w < 1.0$. A uniform z -grid spacing $\Delta z/\delta_{\infty} = 0.727$ was employed. The computation employing the Baldwin-Lomax model utilized a grid of 244,400 points. The x -grid spacing was concentrated near the corner, with a minimum $\Delta x/\delta_{\infty} = 0.157$. The maximum $\Delta x/\delta_{\infty} = 0.515$ and 0.788 at the upstream and downstream boundaries, respectively. The y -grid spacing was concentrated near the surface with the minimum $\Delta y/\delta_{\infty} = 1.03 \times 10^{-3}$, and the maximum $\Delta y/\delta_{\infty} = 0.684$ at

the upper surface GHIJKL. The z-grid spacing was concentrated near the symmetry plane AFEKLG, with a minimum $\Delta z/\delta_\infty = 1.82 \times 10^{-2}$, and a maximum $\Delta z/\delta_\infty = 0.694$ near the boundary BCDJIH.

The results of the three different theoretical models for the $(\alpha, \lambda) = (24, 40)$ deg compression corner at $Re_{\delta_\infty} = 8.1 \times 10^5$ are compared with the experimental data of i) Settles and McKenzie, and ii) Ketchum and Bogdonoff. The computations employing the Cebeci-Smith and Jones-Lauder models utilized a grid of 28,000 points. The x-grid spacing was concentrated near the corner, with a minimum $\Delta x/\delta_\infty = 0.3$, and a maximum $\Delta x/\delta_\infty = 1.0$ at the upstream and downstream boundaries. The y-grid spacing was concentrated near the surface with the minimum $\Delta y/\delta_\infty = 1.02 \times 10^{-4}$, and the maximum $\Delta y/\delta_\infty = 1.0$ at the upper surface GHIJKL. The grid spacing adjacent to the surface satisfied $\Delta y u_\infty / \nu_w < 1.0$. A uniform z-grid spacing $\Delta z/\delta_\infty = 0.6$ was employed. The computation employing the Baldwin-Lomax model utilized a grid of 176,640 points. The x-grid spacing was concentrated near the corner, with a minimum $\Delta x/\delta_\infty = 0.067$. The maximum $\Delta x/\delta_\infty = 0.2$ and 0.335 at the upstream and downstream boundaries, respectively. The y-grid spacing was concentrated near the surface with the minimum $\Delta y/\delta_\infty = 3.4 \times 10^{-4}$, and the maximum $\Delta y/\delta_\infty = 0.467$ at the upper surface GHIJKL. The grid spacing adjacent to the surface satisfied $\Delta y u_\infty / \nu_w < 2.0$. The z-grid spacing was concentrated near the symmetry plane AFEKLG, with a minimum $\Delta z/\delta_\infty = 7.2 \times 10^{-3}$, and a maximum $\Delta z/\delta_\infty = 0.564$ near the boundary BCDJIH.

Comparison with Experiment

$$Re_{\delta_\infty} = 2.6 \times 10^5$$

Experimental profiles of pitot pressure and yaw angle were obtained by Settles and McKenzie¹⁵ at fifteen positions for the $(\alpha, \lambda) = (24, 40)$ swept compression corner at $Re_{\delta_\infty} = 2.6 \times 10^5$. The locations of the measurements are shown in Fig. 4. The profiles were taken at a fixed spanwise position $z = 9.68 \delta_\infty$, and the streamwise positions $(x - x_{\text{corner}})/\delta_\infty = -8.48, -4.85, -4.24, -3.64, -2.73, -0.61, 0, 0.61, 1.52, 3.03, 4.24, 7.27, 9.09, 10.9$, and 14.6 , where $x_{\text{corner}} = z \tan \lambda$ is the location of the corner at a given z . These locations are designated as Positions 1, 2, ..., 15. The profiles for Positions 1 through 9 and

15 were obtained along the vertical axis. The profiles for Positions 10 through 14 were taken along a line tilted upstream at an angle $\gamma = 16$ deg.

A set of four pitot pressure and yaw angle profiles have been selected for presentation. The position locations were chosen based upon two criteria, namely, i) the comparison between the computed and experimental profiles is indicative of the full set of fifteen profiles, and ii) the positions were located near identifiable features of the flow (i.e., the line of coalescence, the corner line, the line of divergence, and a position far downstream). The pitot profiles at Position 5, located approximately at the line of coalescence, are displayed in Fig. 5. The horizontal axis is the pitot pressure p_p normalized by the upstream freestream pitot pressure p_{p_∞} . The vertical axis is the distance measured from the surface (see above), normalized by the upstream boundary layer thickness δ_∞ . The experimental profile displays an approximate 40% overshoot in p_p at the edge of the boundary layer. This overshoot is associated with the compression region upstream of the interaction.²³⁻²⁵ It is evident to a lesser extent in the calculations employing the Cebeci-Smith and Jones-Lauder models, and is absent from Baldwin-Lomax computation. The underestimate of the pitot pressure overshoot is attributable to the underprediction of the upstream influence of the interaction by all three models. This underprediction is also apparent in the computed surface pressure profiles (see below).

The pitot profiles at Position 7, located at the corner line, are shown in Fig. 6. Good agreement is observed between the computed and measured profiles, with discrepancies limited to the vicinity of the shock wave at $y = 2.5 \delta_\infty$ where the computed profiles underpredict the height of the shock wave. The underprediction is another manifestation of the underestimate of the upstream influence of the interaction (i.e., the computed shock structure is situated downstream of the experimental shock structure). The pitot profiles at Position 10, located approximately at the line of divergence, are displayed in Fig. 7. The three computed profiles are very similar, and in good agreement with experiment. The pitot profiles at Position 14, located far downstream, are shown in Fig. 8. Good agreement between the calculated and measured

profiles is again observed.

The yaw angle profiles at the same four Positions are displayed in Figs. 9 to 12. The yaw angle β is defined as $\beta = \tan^{-1}(w/(u \cos \gamma + v \sin \gamma))$, where (u, v, w) are the Cartesian velocity components in the (x, y, z) coordinate system, and γ is the angle of tilt of the measured profile (see above). Near the line of coalescence (Fig. 9), the yaw angle is observed to be small except in the immediate vicinity of the surface. The computed profiles display significant differences near the wall. The proximity of this position to the line of coalescence accentuates the differences between the three models, since the near-surface yaw angle at a fixed height is observed to increase rapidly as the line of coalescence is approached from upstream. The yaw angle profiles at the corner line (Fig. 10) show close agreement between the three models. The experimental data is limited to $y > \delta_\infty$ due to the size of the boundary layer and the probe geometry. Near the line of attachment (Fig. 11), the computed profiles are nearly identical, and display generally good agreement with experiment. Finally, the computed and measured yaw angle profiles far downstream (Fig. 12) show close agreement.

The computed and measured surface pressure profiles at $z = 10.18\delta_\infty$ are shown in Fig. 13. There is general agreement between the calculated and experimental profiles, although the data is limited to points upstream of the corner line. The computations using the Baldwin-Lomax model modestly underpredict the upstream influence (i.e., the location of the initial pressure rise). Additional data at $z = 14.68\delta_\infty$ exhibit a similar behavior. The calculations utilizing the Cebeci-Smith and Jones-Lauder models show closer agreement with experiment. These computations utilized a coarser grid, however, and further calculations are needed to determine the effect of grid refinement.

$$Re_{\delta_\infty} = 8.1 \times 10^5$$

Experimental profiles of pitot pressure and yaw angle were obtained by Settles and McKenzie¹⁵ at fifteen stations for the $(\alpha, \lambda) = (24, 40)$ swept compression corner at $Re_{\delta_\infty} = 8.1 \times 10^5$. The locations of the measurements are shown in Fig. 4. The profiles were taken at a fixed span-

wise position $z = 7\delta_\infty$, and streamwise positions $(x - x_{\text{corner}})/\delta_\infty = -4, -3.2, -2.8, -2.4, -2, -1.4, -0.8, -0.2, 1.4, 2.6, 3, 3.6, 4.2, 4.8, \text{ and } 6$. Experimental profiles of pitot pressure, yaw angle and static pressure were obtained by Ketchum and Bogdonoff for the same configuration at $z = 7\delta_\infty$, and streamwise positions $(x - x_{\text{corner}})/\delta_\infty = -4.0, -2.8, -1.4, -0.8, 0.4, 1.6, 2.4, 3.6, 4.8, 6.0$ and 8.4. The resolution of these profiles (i.e., the number of experimental data points within the boundary layer) was greater than the previous measurements of Settles and McKenzie. Seven of the positions of Ketchum and Bogdonoff coincide with the Settles and McKenzie data. The two sets of data display close agreement at these positions, thereby verifying the repeatability of the experiments which were performed several years apart. The two data sets have been merged into a single data set of nineteen positions at $(x - x_{\text{corner}})/\delta_\infty = -4, -3.2, -2.8, -2.4, -2, -1.4, -0.8, -0.2, 0.4, 1.4, 1.6, 2.4, 2.6, 3.0, 3.6, 4.2, 4.8, 6.0, \text{ and } 8.4$. The profiles for Positions 1 through 9, 11 and 12 were obtained along the vertical axis. The profiles for Positions 10 and 13 through 17 were obtained along a line tilted upstream at an angle $\gamma = 16$ deg. The profiles for Positions 18 and 19 were taken at $\gamma = 24$ deg. The experimental line of coalescence¹⁵ is observed at $x - x_{\text{corner}} = -2.5\delta_\infty$ for $z = 7\delta_\infty$, located between Positions 3 and 4. The experimental line of divergence is found at $x - x_{\text{corner}} = 2.6\delta_\infty$ for $z = 7\delta_\infty$, located at Position 13.

A set of four pitot pressure and yaw angle positions have been selected for presentation using the same criteria employed for $Re_{\delta_\infty} = 2.6 \times 10^5$. In Fig. 14, computed and experimental pitot pressure profiles are displayed at Position 4, located slightly downstream of the experimental line of coalescence. The profiles are in close agreement, and display negligible effect of the interaction. The computed and measured profiles at Position 9, located $0.4\delta_\infty$ downstream of the corner, are displayed in Fig. 15. The calculated profiles agree closely with the experimental data within the boundary layer, with the Baldwin-Lomax model providing a slightly improved prediction. Outside the boundary layer, the computed profiles display a diffused profile in the vicinity of the shock wave due to the shock-capturing nature of the numerical algorithms. The computed and experimental pitot pressure profiles at Position 13, located at the

line of divergence, are shown in Fig. 16. The profiles display excellent agreement, and show negligible variation due to the turbulence model. Finally, the calculated and measured profiles at Position 18, located downstream of the line of divergence, are shown in Fig. 17. Close agreement is again observed between the computed and measured profiles.

The yaw angle profiles at the same four positions are displayed in Figs. 18 to 21. The computed and measured yaw angle at Position 4, located slightly downstream of the line of coalescence, display negligible yaw angle except within the immediate vicinity of the surface. There is considerable discrepancy between the calculated and measured surface yaw angles at this position due to the differences in the calculated upstream influence (see below). The calculated and experimental yaw angles at Position 9, located 0.48_m downstream of the corner, are shown in Fig. 19. The computed yaw angle profiles are virtually identical, indicating insensitivity to the turbulence model employed. The computed profiles overpredict the experimental yaw angle profile of Ketchum and Bogdonoff in the outer portion of the boundary layer. The computed and measured yaw angle profiles at Position 13, located at the line of divergence, are displayed in Fig. 20. The calculated profiles are seen to be virtually identical, and in close agreement with experiment. Finally, the yaw angle profiles at Position 18, located downstream of the line of divergence, are presented in Fig. 21. Excellent agreement is observed between the calculated profiles and experiment.

The computed and measured surface pressure profiles at $z = 105_{mm}$ are shown in Fig. 22. The calculated profile using the Baldwin-Lomax model underpredicts the upstream influence (i.e., the location of the initial pressure rise). This behavior has been observed previously in a variety of 3-D shock wave-turbulent boundary layer computations using the Baldwin-Lomax model.¹¹⁻¹⁴ The plateau pressure is accurately predicted. The calculated profiles using the Cebeci-Smith and Jones-Launder models provide a more accurate prediction of the upstream influence, but significantly overpredict the plateau pressure. Further investigation of the effect of grid refinement for the calculations using the Cebeci-Smith and Jones-Launder models is required.

Flowfield Structure

The general agreement between computed and experimental pitot pressure and yaw angle profiles for the $(\alpha, \lambda) = (24, 40)$ deg configuration (see above) and the $(\alpha, \lambda) = (24, 60)$ deg configuration¹⁴ permits the development of flowfield models based on the computed results. The calculated profiles of pitot pressure and yaw angle have been observed to be insensitive to the turbulence model employed, except within the immediate vicinity of the surface (e.g., typically the lower 10% of the boundary layer). It suffices, therefore, to examine the flowfield structure using the computed flowfields of a single turbulence model (e.g., Baldwin-Lomax), with the understanding that some quantitative differences will appear near the surface. The present paper, therefore, focuses on a detailed quantitative study of the flowfield structure for the $(\alpha, \lambda) = (24, 40)$ and $(24, 60)$ deg configurations using the computed flowfields with the Baldwin-Lomax model.

The computed surface skin friction lines for the $(\alpha, \lambda) = (24, 40)$ configuration are displayed in Figs. 23 and 24 for $Re_{\infty} = 2.6 \times 10^5$ and 8.1×10^5 , respectively. The line of coalescence, formed by the convergence of the upstream skin friction lines, is clearly evident. Results for the $(\alpha, \lambda) = (24, 60)$ configuration¹⁴ indicated that angle of the computed line of coalescence, measured relative to the spanwise direction z , was approximately 10% greater than the experimental value based upon kerosene lampblack surface visualization. The line of divergence, situated on the compression surface, is also shown.

The flowfield structures for the $(\alpha, \lambda) = (24, 40)$ deg and $(24, 60)$ deg configurations are similar. A general mean flowfield model, developed on the basis of particle pathlines¹⁴, is presented in Fig. 25. It is emphasized that this is a model based upon the *mean* flowfield, whereas in the actual experiment the flowfield is turbulent and therefore unsteady. The principal element of the flow is a large vortical structure. The line of coalescence defines the origin of a three dimensional surface of separation, denoted as Surface No. 1. The surface spirals into the core of the vortical structure. It should be noted, however, that the streamlines comprising Surface No. 1 exhibit a significant yaw angle, and consequently are skewed strongly in the spanwise

direction. Approaching the line of coalescence, the streamlines close to the surface rise moderately and move strongly in the spanwise direction. At the computed line of coalescence for $z = 7\delta_\infty$, for example, the maximum angle of pitch (defined as $\tan^{-1}(v/\sqrt{u^2 + w^2})$) is approximately 4 deg and occurs at $y = 0.128\delta_\infty$; the maximum yaw angle is 60 deg and occurs at the surface. The line of divergence defines the intersection of a second surface, denoted as Surface No. 2, with the swept compression ramp. This second surface extends upstream into the undisturbed flow. The fluid contained between the wall and Surface No. 2 becomes the vortical structure, which is approximately aligned with the corner. The fluid above the second surface passes over the vortical structure and continues up the compression ramp.

A quantitative measure of the Surface No. 1 is its angle of intersection with the wall, measured in a plane orthogonal to the line of coalescence. The calculated angle is 10 ± 2 deg for the $(\alpha, \gamma) = (24, 40)$ deg configuration at $Re_{\delta_\infty} = 2.6 \times 10^5$ and 8.1×10^5 . The same value is obtained for the $(24, 60)$ deg configuration at $Re_{\delta_\infty} = 1.4 \times 10^5$ and 9×10^5 . The angle of intersection is not, however, the angle of pitch of the streamlines comprising Surface No. 1. Those streamlines are moving spanwise in a direction approximately aligned with the line of coalescence, and therefore their pitch is less than the angle of intersection of Surface No. 1 with the wall.

An important feature of Surface No. 2 is its height above the wall, measured at a fixed streamwise position immediately upstream of the interaction. The calculated height of Surface No. 2 is displayed in Fig. 26 for $(\alpha, \gamma) = (24, 40)$ deg at $Re_{\delta_\infty} = 2.6 \times 10^5$ and 8.1×10^5 , and for $(\alpha, \lambda) = (24, 60)$ deg configuration at $Re_{\delta_\infty} = 1.4 \times 10^5$ and 9×10^5 . The height of Surface No. 2 at a given spanwise location z is determined by examining streamlines originating at various values of y , and observing whether the particular streamline moves up along the compression surface or spirals into the vortical structure. The height is defined as the limit where the streamlines approach the line of divergence and move parallel to it. As the value of z increases, greater uncertainty arises in determining whether a streamline is moving up the ramp or into the vortex. This increasing uncertainty is associated

with the limited spanwise extent of the computational domain to view the particular streamline. Consequently, there are two lines shown for each value of (α, λ) and Re_{δ_∞} . These lines represent the upper and lower estimates of the height of Surface No. 2.

There are two important features regarding the height of Surface No. 2. First, the height for the $(\alpha, \lambda) = (24, 40)$ deg configuration appears to asymptote at $y = 0.158\delta_\infty$, while for the $(\alpha, \lambda) = (24, 60)$ deg configuration the height continues to increase in an approximate linear manner well beyond $y = \delta_\infty$. The limited spanwise extent of the computations precludes a definitive statement regarding the asymptotic behavior of the characteristics of the computed flowfields including the height of Surface No. 2 and the nature of the line of coalescence. Settles and Teng²⁶ classified both the $(\alpha, \lambda) = (24, 40)$ and $(24, 60)$ configurations as "conical" in the sense that the line of coalescence was determined to asymptote a straight line at a fixed angle relative to the corner line, whereas Wang and Bogdonoff²⁷ suggested that the farfield behavior would always approach cylindrical flow. The relationship between the asymptotic behavior of the line of coalescence and the height of Surface No. 2 is not understood at present, and is the topic of further investigation. Second, the results for the two different Reynolds numbers at each (α, λ) indicate that the height appears to scale with the upstream boundary layer thickness. McClure and Dolling²⁵ suggested that the flowfield structure of the 3-D sharp fin at $\alpha = 10$ deg, Mach 3 and $Re_{\delta_\infty} = 3.2 \times 10^5$ and 7.9×10^5 scaled according to $(y/\delta_0)Re_{\delta_0}^{-1/3}$ vs. $(z/\delta_0)Re_{\delta_0}^{-1/3}$ based upon surface measurements of the 3-D swept compression corner at similar flow conditions by Settles and Bogdonoff²⁸, where δ_0 is the local incoming boundary layer thickness. The present computations, although limited in spanwise extent, do not support the flowfield scaling model of McClure and Dolling.

Further understanding of the flowfield structure may be obtained through examination of the governing equations, specifically, the evaluation of the various terms in the governing equations along a streamline. The mean kinetic energy per unit mass ("mechanical energy") is examined for simplicity. The equation is

$$D(\frac{1}{2}u_i u_i)/Dt = -(u_i/\rho)\partial p/\partial x_i + (u_i/\rho)\partial \tau_{ij}/\partial x_j$$

where $\frac{1}{2}u_i u_i$ is the mean kinetic energy per unit mass, $D/Dt = \partial/\partial t + u_j \partial/\partial x_j$, $(u_1, u_2, u_3) = (u, v, w)$, $(x_1, x_2, x_3) = (x, y, z)$, p is the static pressure, ρ is the density, τ_{ij} is the total (viscous plus turbulent) stress tensor, and the Einstein summation convention is employed. There are two contributions to the rate of change of the mean kinetic energy per unit mass. The first term, $-(u_i/\rho)\partial p/\partial x_i$, is an inviscid effect associated with compression or dilation. The second term, $(u_i/\rho)\partial \tau_{ij}/\partial x_j$, represents the effect of the viscous and turbulent stresses. A series of flow streamlines are generated by integrating the motion of a fluid particle, released at a selected upstream position, through the computed flowfield. The mean kinetic energy equation is integrated simultaneously along the streamline, i.e.,

$$\frac{1}{2}u_i u_i = \frac{1}{2}u_i u_i|_0 + \int \{ -(u_i/\rho)\partial p/\partial x_i + (u_i/\rho)\partial \tau_{ij}/\partial x_j \} ds/V$$

where $\frac{1}{2}u_i u_i|_0$ is the initial mean kinetic energy at the point of release of the fluid particle, ds is the infinitesimal arclength along the streamline and $V = \sqrt{u_i u_i}$. The separate contributions of the integrands $-(u_i/\rho)\partial p/\partial x_i$ and $(u_i/\rho)\partial \tau_{ij}/\partial x_j$ provide a quantitative measure of the inviscid and viscous contributions to the rate of change of the mean kinetic energy.

The contributions to the rate of change of the mean kinetic energy are evaluated for the $(\alpha, \lambda) = (24, 40)$ deg configuration at $Re_{\delta_{99}} = 8.1 \times 10^5$ from the calculated flowfield obtained using the Baldwin-Lomax model. A series of ten streamlines, released within the upstream undisturbed boundary layer at $y = 0.02\delta_{99}$, are displayed in Fig. 27. The entrainment of the streamlines into the vortical structure is clearly evident. The mean kinetic energy on the fifth streamline (counted from the plane of symmetry) is presented in Fig. 28 as a function of arclength along the streamline. The figure displays both the integrated kinetic energy, obtained from the path integral of the mean kinetic energy equation (see above), and the interpolated kinetic energy, obtained from interpolation of the computed flowfield. These two results are not identical, due to the truncation errors of the numerical computation of both the flowfield and the path integral. The results, however, are seen to be in close agreement. The kinetic energy decreases abruptly at the start of

the interaction, reaches a minimum value shortly after entering the vortical structure, and eventually asymptotes a nearly constant value. In Fig. 29, two profiles are displayed for this streamline. The first profile, denoted the "Pressure and Viscous Contribution", is the integrated mean kinetic energy displayed previously in Fig. 28, i.e., the path integral of the mean kinetic energy equation obtained by including *both the pressure and viscous integrands*, i.e., $-(u_i/\rho)\partial p/\partial x_i$ and $(u_i/\rho)\partial \tau_{ij}/\partial x_j$. The second profile, denoted the "Pressure Contribution", is the path integral of the mean kinetic energy equation obtained by including *only the pressure integrand*, i.e., $-(u_i/\rho)\partial p/\partial x_i$. The two profiles are observed to be significantly different, and it is therefore concluded that *both* inviscid and viscous effects are important for this particular streamline. Similar results are observed for the other nine streamlines emanating at $y = 0.02\delta_{99}$.

In Fig. 30, a series of ten streamlines, released at $y = 0.05\delta_{99}$, are displayed. The streamlines roll up into the vortical structure as expected from Fig. 26. The interpolated and integrated kinetic energy for the fifth streamline, displayed in Fig. 31, are in close agreement. The profiles in Fig. 32 display the mean kinetic energy of the fifth streamline obtained from the path integral of the pressure and viscous contributions, and from the path integral of the pressure contribution alone. *The integrated mean kinetic energy, obtained from the path integral of the pressure contribution alone, provides a reasonably accurate measure of the kinetic energy.* This implies, therefore, that the turbulent stresses have a minimal effect on the evolution of these streamlines, *despite their origin deep within the boundary layer at $y = 0.05\delta_{99}$ and their entrainment within the vortical structure.* Similar results are observed for the other nine streamlines emanating at $y = 0.05\delta_{99}$.

In Fig. 33, the final series of ten streamlines, released at $y = 0.5\delta_{99}$, are shown. These streamlines move over the vortical structure, and continue up along the ramp (Fig. 26). The integrated and interpolated mean kinetic energy for the fifth streamline, displayed in Fig. 34, show a discrepancy of approximately 18%. Further investigations are in progress to examine this effect. The profiles in Fig. 34 display the mean kinetic energy of the fifth streamline obtained from the path integral of the pressure

and viscous contributions, and the path integral of the pressure contribution alone. It is again observed that the mean kinetic energy obtained from the path integral of the pressure contribution *alone* is a reasonable prediction, varying from the full interpolated kinetic energy by only 15%. Similar results are observed for the other nine streamlines emanating at $y = 0.5\delta_{\infty}$. It is again evident that turbulent stresses play a minor role in the dynamics of the fluid motion for these streamlines.

The examination of the mean kinetic energy for the $(\alpha, \lambda) = (24, 40)$ deg configuration at $Re_{\delta_{\infty}} = 8.1 \times 10^5$ provides a quantitative indication of the importance of inviscid and viscous effects. Except in the immediate vicinity of the surface, the flowfield is observed to be rotational and inviscid, as conjectured previously for the 3-D sharp fin.¹³ Further investigations are in progress for other swept compression corner configurations.

Conclusions

A collaborative experimental and theoretical research program has focused on the 3-D shock wave-turbulent boundary layer interaction generated by a swept compression corner, characterized by the compression angle α and the sweep angle λ . In the present effort, computations have been performed for $(\alpha, \lambda) = (24, 40)$ deg at $Re_{\delta_{\infty}} = 2.6 \times 10^5$ and 8.1×10^5 at Mach 3 using the Baldwin-Lomax turbulence model. These results are compared with the experimental data of Settles and McKenzie, Ketchum and Bogdonoff, and previous computations by Horstman using the Cebeci-Smith and Jones-Launder turbulence models. The calculated and experimental profiles of pitot pressure and yaw angle are in good agreement. The computed profiles are remarkably insensitive to the turbulence model employed except in a narrow region comprising the lower 10% of the boundary layer where differences of 10%-20% in yaw angle are observed. The calculated surface pressure using the Baldwin-Lomax underpredicts the location of upstream influence, although providing reasonable agreement elsewhere. The computed surface pressure using the Cebeci-Smith and Jones-Launder models provides a better prediction of the upstream influence point, but overpredict the pressure in the vicinity of the corner. Further calculations using the Cebeci-Smith and Jones-Launder models are required to ascertain the

effects of grid resolution.

The dominant feature of the $(\alpha, \lambda) = (24, 40)$ deg flowfield is a large vortical structure, approximately aligned with the corner, similar to the flow structure for the $(\alpha, \lambda) = (24, 60)$ deg configuration. A surface of streamlines emanates from the line of coalescence, and forms the core of the vortical structure. The surface intersects the wall at an angle of 10 ± 2 deg for both configurations. The angle of intersection is not, however, the angle of pitch of the streamlines comprising Surface No. 1. Those streamlines are moving spanwise in a direction approximately aligned with the line of coalescence, and their pitch is therefore less than the angle of intersection of Surface No. 1 with the wall. A second surface originates upstream within the boundary layer and intersects the compression ramp at the line of divergence. The fluid contained between the wall and the second surface is entrained into the vortical structure. The height of the surface, measured immediately upstream of the interaction, is strongly dependent on the sweepback angle λ and scales with the upstream boundary δ_{∞} .

The mean kinetic energy equation is examined for a series of streamlines emanating within the upstream boundary layer for the $(\alpha, \lambda) = (24, 40)$ deg configuration at $Re_{\delta_{\infty}} = 8.1 \times 10^5$. Three initial heights were selected, namely, $y/\delta_{\infty} = 0.02, 0.05$ and 0.5 . The change of kinetic energy along streamlines emanating from $y = 0.02\delta_{\infty}$ was observed to be influenced strongly by both inviscid and viscous effects. However, for the streamlines originating at $y/\delta_{\infty} = 0.05$ and 0.5 , the rate of change of kinetic energy was attributable almost entirely to inviscid effects. The streamlines emanating at $y = 0.05\delta_{\infty}$ were entrained within the vortical structure, while the streamlines originating at $y = 0.5\delta_{\infty}$ moved over the vortical structure and up along the compression surface. This represents the first direct indication that the vortical structure is predominantly rotational and inviscid, except within a very narrow region of the boundary layer adjacent to the wall.

Acknowledgments

This research is sponsored by the Air Force Office of Scientific Research under AF Grant 86-0266 and AF Contract F49620-86-C-0094, monitored by Drs. James Wilson and Jim

McMichael, the NASA Ames Research Center, and the National Science Foundation. The first author expresses his appreciation to Mr. Dias Badekas for his development of graphics programs on the Sun workstations and preparation of several plots, to Mr. Natraj Narayanswami for his development of the program to analyze the contributions to the rate of change of kinetic energy along streamlines and preparations of several plots, and to Mr. Yan Zang for the preparation of several color viewgraphs using MOVIE.BYU.

The computations were performed on the CYBER 205 at the John von Neumann Center, Princeton, NJ, and the CRAY X-MP 4/8 at the NASA Ames Research Center, Moffett Field, CA.

References

1. Ferri, A., "Experimental Results with Airfoils Tested in the High-Speed Tunnel at Guidonia", NASA TM 946 (translation), 1940.
2. Settles, G., and Dolling, D., "Swept Shock Wave Boundary-Layer Interactions", in *Tactical Missile Aerodynamics*, AIAA Progress in Astronautics and Aeronautics Series, Vol. 104, 1986, pp. 297-379.
3. Liepmann, H., "The Interaction Between Boundary Layer and Shock Waves in Transonic Flow", *J. Aero. Sciences*, Vol. 13, pp. 623-637, 1946.
4. Ackeret, J., Feldman, F., and Rott, N., "Investigations of Compression Shocks and Boundary Layers in Gases Moving at High Speeds", NASA TM 1113, 1947.
5. Greene, J., "Interactions Between Shock Waves and Turbulent Boundary Layers", *Progress in Aerospace Sciences*, Vol. 11, Pergamon Press, 1970, pp. 235-341.
6. Baldwin, B., and Lomax, H., "Thin Layer Approximation and Algebraic Model for Separated Turbulent Flows", AIAA Paper 78-257, 1978.
7. Cebeci, T., and Smith, A.M.O., *Analysis of Turbulent Boundary Layers*, Academic Press, New York, 1974.
8. Jones, W., and Launder, B., "The Prediction of Laminarization with a Two-Equation Model of Turbulence", *Int. J. Heat and Mass Transfer*, Vol. 15, 1972, pp. 301-304.
9. Horstman, C., and Hung, C., "Computation of Three-Dimensional Separated Flows at Supersonic Speeds", AIAA Paper No. 79-0002, 1979.
10. Knight, D., "A Hybrid Explicit-Implicit Numerical Algorithm for the Three-Dimensional Compressible Navier-Stokes Equations", *AIAA J.*, Vol. 22, 1984, pp. 1056-1061.
11. Knight, D., "Modelling of Three-Dimensional Shock Wave Turbulent Boundary Layer Interactions", Workshop on Macroscopic Modelling of Turbulent Flows and Fluid Mixtures, INRIA, Nice, France, December 1984; also, *Lecture Notes in Physics*, Springer-Verlag, Vol. 230, 1985, pp. 177-201.
12. Knight, D., "Numerical Simulation of 3-D Shock Turbulent Boundary Layer Interaction Generated by a Sharp Fin", *AIAA J.*, Vol. 23, No. 12, December 1985, pp. 1885-1891.
13. Knight, D., Horstman, C., Shapey, B., and Bogdonoff, S., "The Flowfield Structure of the 3-D Shock Wave-Boundary Layer Interaction Generated by a 20 deg Sharp Fin at Mach 3", *AIAA J.*, Vol. 25, No. 10, October 1987, pp. 1331-1337.
14. Knight, D., Horstman, C., Ruderich, R., Mao, M.-F., and Bogdonoff, S., "Supersonic Turbulent Flow Past a 3-D Swept Compression Corner at Mach 3", AIAA Paper No. 87-0551, 1987.
15. Settles, G., Horstman, C. and McKenzie, T., "Experimental and Computational Study of a Swept Compression Corner Interaction Flowfield", *AIAA J.*, Vol. 24, May 1986, pp. 744-752.
16. Vas, I., and Bogdonoff, S., "A Preliminary Report on the Princeton University High Reynolds Number 8 inch by 8 inch Supersonic Tunnel", Aerospace and Mechanical Sciences Internal Memorandum No. 39, Princeton University, 1971.
17. Settles, G., "An Experimental Study of Compressible Turbulent Boundary Layer Separation at High Reynolds Number", PhD Thesis, Department of Aerospace and Mechanical Engineering, Princeton University, 1975.
18. Settles, G., Perkins, J., and Bogdonoff, S., "Upstream Influence Scaling of 2D and 3D Shock/Turbulent Boundary Layer Interactions at Compression Corners", *AIAA J.*, Vol. 20, 1982, pp. 782-789.
19. Sun, C.-C., and Childs, M., "Wall Wake Velocity Profile for Compressible Nonadiabatic Flows", *AIAA J.*, Vol. 14, 1976, pp. 820-822.
20. Rubesin, M., and Rose, W., "The Turbulent Mean-Flow, Reynolds-Stress and Heat-Flux Equations in Mass Averaged Dependent Variables", NASA TMX-62248, 1973.

21. Pulliam, T. and Steger, J., "Implicit Finite-Difference Simulations of Three-Dimensional Compressible Flow", *AIAA J.*, Vol. 18, 1980, pp. 159-167.
22. MacCormack, R., "A Numerical Method for Solving the Equations of Viscous Compressible Flow", *AIAA J.*, Vol. 20, 1982, pp. 1275-1281.
23. Oskam, B., Vas, I., and Bogdonoff, S., "Mach 3 Oblique Shock Wave/Turbulent Boundary Layer Interactions in Three Dimensions", AIAA Paper No. 76-336, 1976.
24. Oskam, B., Vas, I., and Bogdonoff, S., "An Experimental Study of Three-Dimensional Flow Fields in an Axial Corner at Mach 3", AIAA Paper No. 77-689, 1977.
25. McClure, W., and Dolling, D., "Flowfield Scaling in Sharp-Fin Induced Shock Wave Turbulent Boundary Layer Interaction", AIAA Paper No. 83-1754, 1983.
26. Settles, G., and Teng, H.-Y., "Cylindrical and Conical Flow Regions of Three-Dimensional Shock/Boundary Layer Interactions", *AIAA J.*, Vol. 22, Feb 1984, pp. 194-200.
27. Wang, S., and Bogdonoff, S., "A Re-Examination of the Upstream Influence Scaling and Similarity Laws for 3-D Shock Wave/Turbulent Boundary Layer Interaction", AIAA Paper No. 86-0347, 1986.
28. Settles, G., and Bogdonoff, S., "Scaling of Two- and Three-Dimensional Shock/Turbulent Boundary-Layer Interactions at Compression Corners", *AIAA J.*, Vol. 20, June 1982, pp. 782-789.

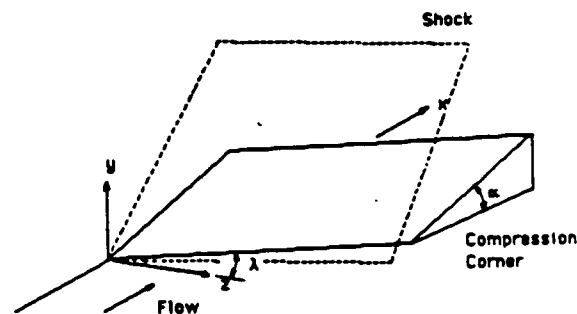


Fig. 2 3-D Swept compression corner

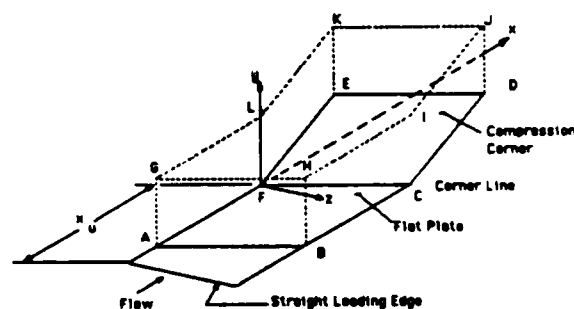


Fig. 3 Computational domain for 3-D swept compression corner

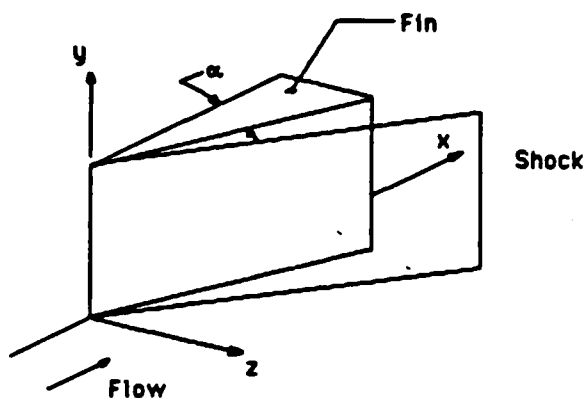


Fig. 1 3-D Sharp fin

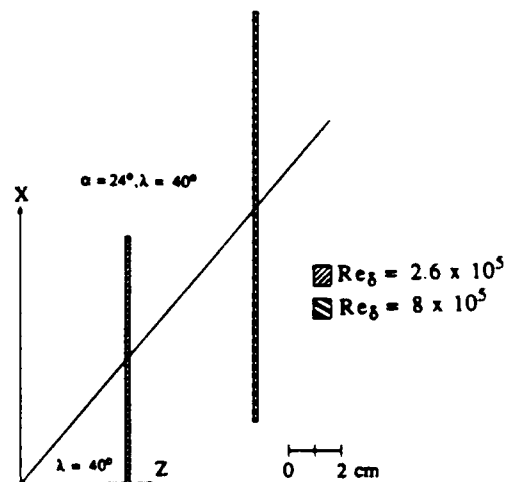


Fig. 4 Location of pitot pressure and yaw measurements

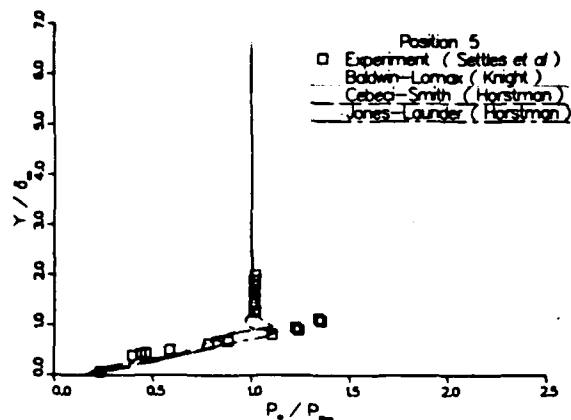


Fig. 5 Pitot pressure at Position 5 for $Re_{\delta_{99}} = 2.6 \times 10^5$

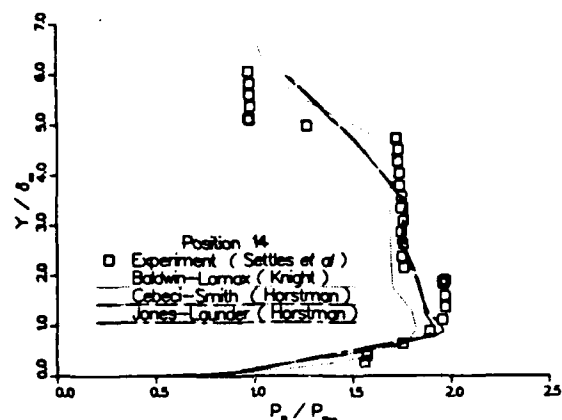


Fig. 8 Pitot pressure at Position 14 for $Re_{\delta_{99}} = 2.6 \times 10^5$

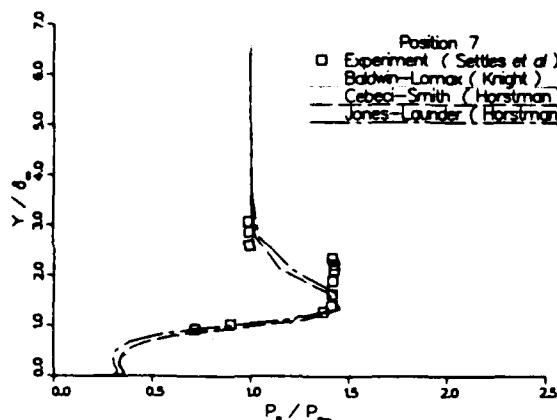


Fig. 6 Pitot pressure at Position 7 for $Re_{\delta_{99}} = 2.6 \times 10^5$

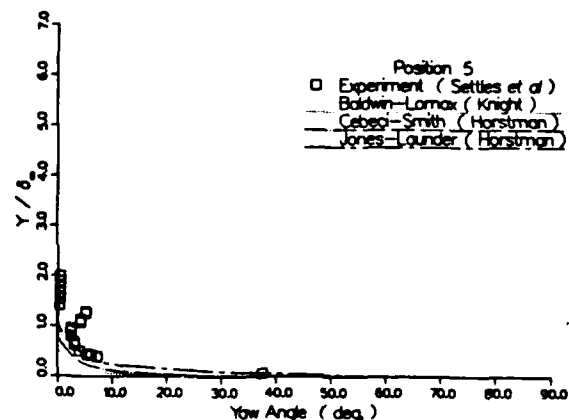


Fig. 9 Yaw angle at Position 5 for $Re_{\delta_{99}} = 2.6 \times 10^5$

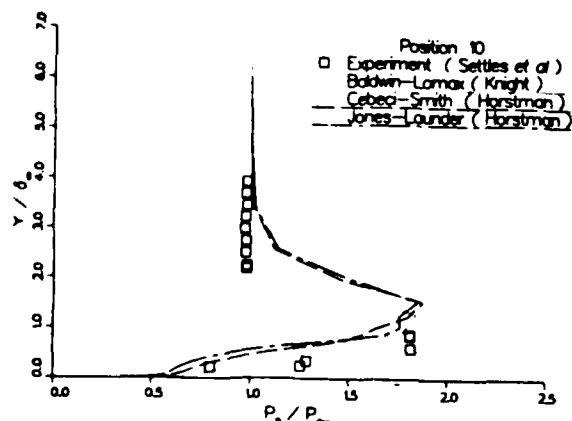


Fig. 7 Pitot pressure at Position 10 for $Re_{\delta_{99}} = 2.6 \times 10^5$

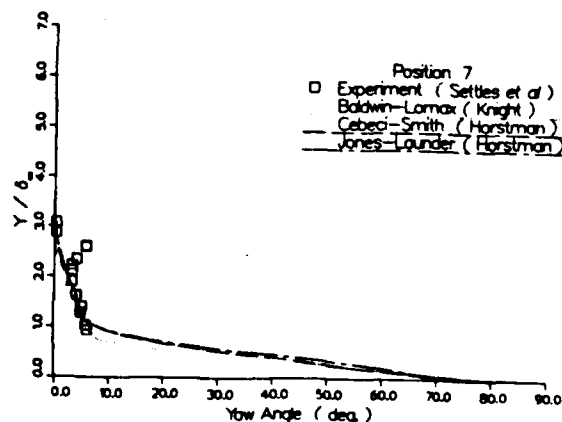


Fig. 10 Yaw angle at Position 7 for $Re_{\delta_{99}} = 2.6 \times 10^5$

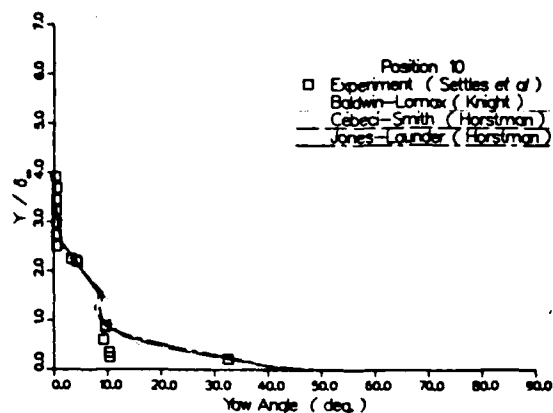


Fig. 11 Yaw angle at Position 10 for $Re_{\delta_{\infty}} = 2.6 \times 10^5$

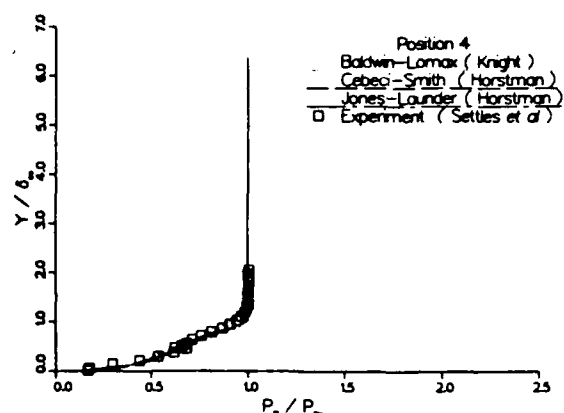


Fig. 14 Pitot pressure at Position 4 for $Re_{\delta_{\infty}} = 8.1 \times 10^5$

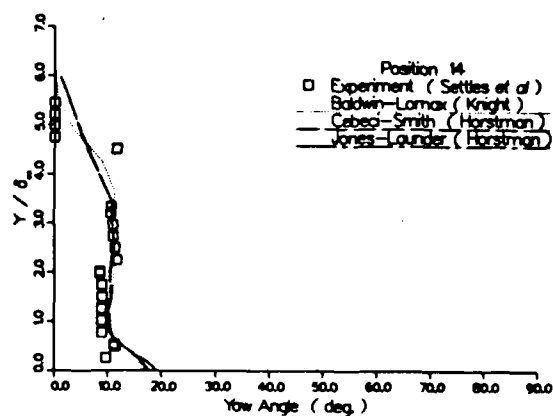


Fig. 12 Yaw angle at Position 14 for $Re_{\delta_{\infty}} = 2.6 \times 10^5$

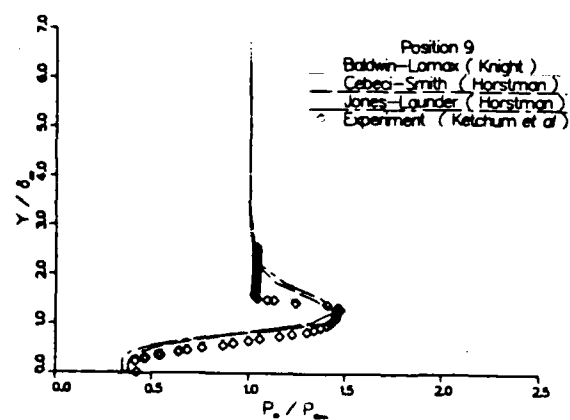


Fig. 15 Pitot pressure at Position 9 for $Re_{\delta_{\infty}} = 8.1 \times 10^5$

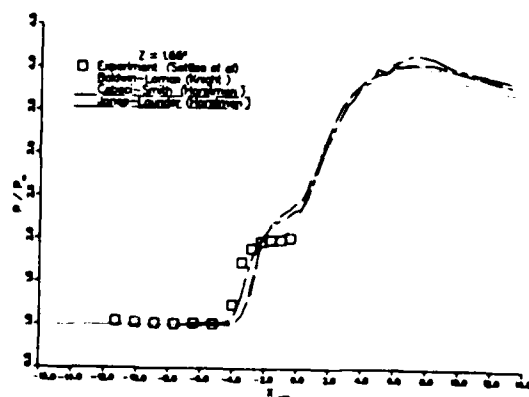


Fig. 13 Surface Pressure at $x = 10.15_{\infty}$ for $Re_{\delta_{\infty}} = 2.6 \times 10^5$

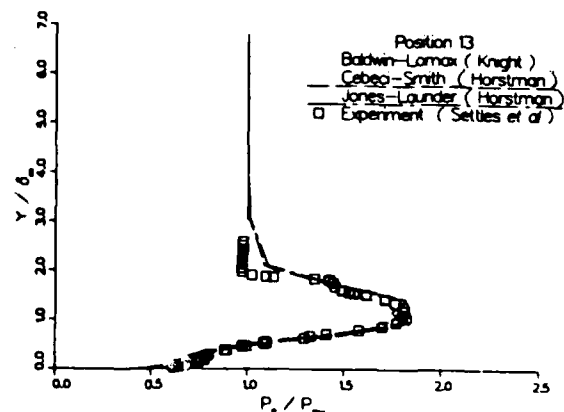


Fig. 16 Pitot pressure at Position 13 for $Re_{\delta_{\infty}} = 8.1 \times 10^5$

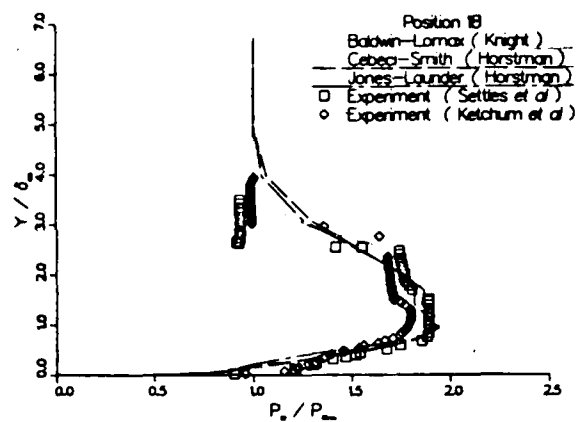


Fig. 17 Pitot pressure at Position 18 for $Re_{\delta_{\infty}} = 8.1 \times 10^5$

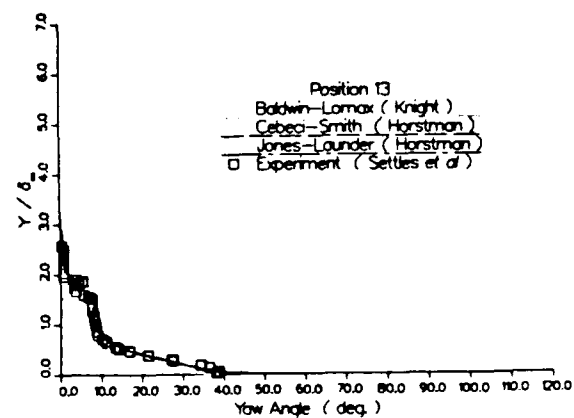


Fig. 20 Yaw angle at Position 13 for $Re_{\delta_{\infty}} = 8.1 \times 10^5$

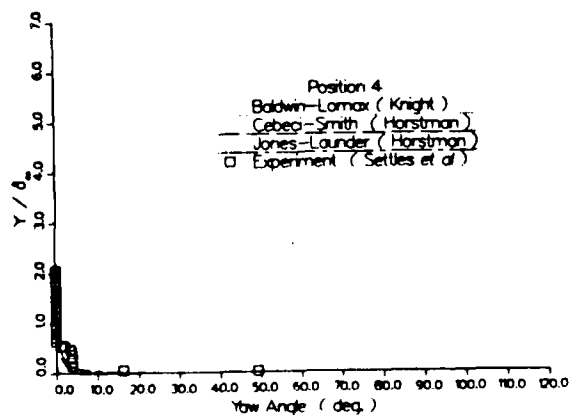


Fig. 18 Yaw angle at Position 4 for $Re_{\delta_{\infty}} = 8.1 \times 10^5$

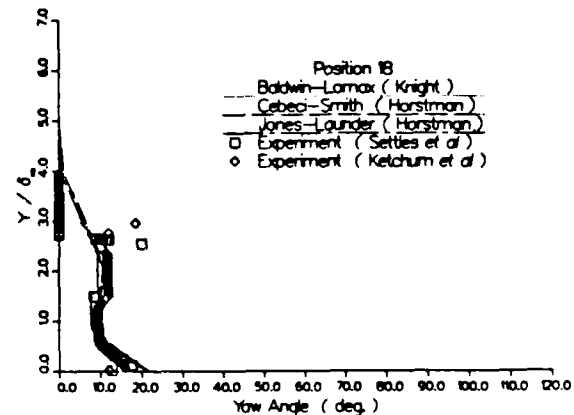


Fig. 21 Yaw angle at Position 18 for $Re_{\delta_{\infty}} = 8.1 \times 10^5$

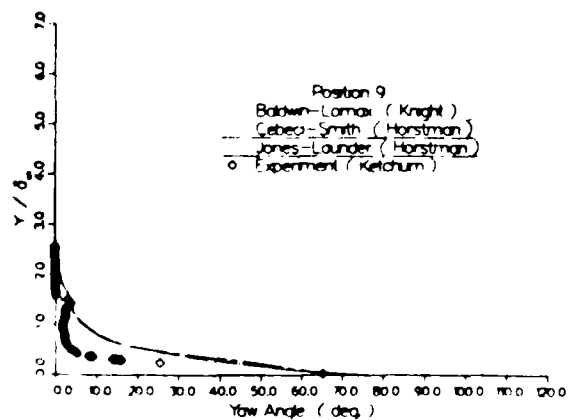


Fig. 19 Yaw angle at Position 9 for $Re_{\delta_{\infty}} = 8.1 \times 10^5$

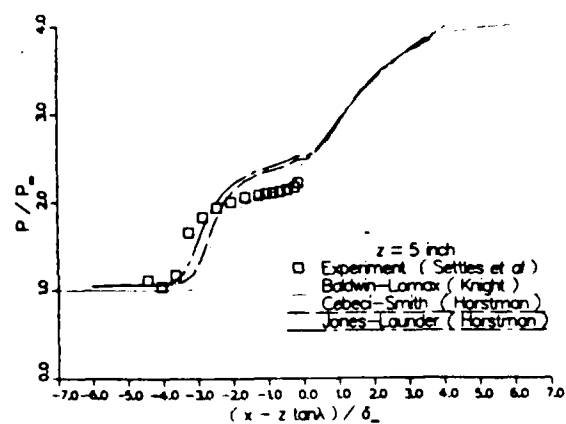


Fig. 22 Surface Pressure at $z = 10.1\delta_{\infty}$ for $Re_{\delta_{\infty}} = 8.1 \times 10^5$

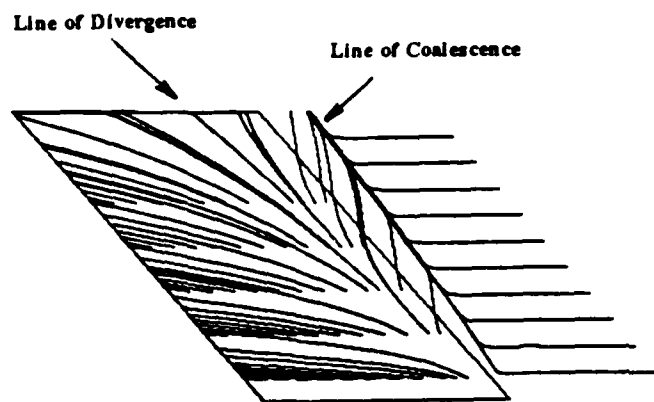


Fig. 23 Computed surface skin friction lines for $Re_{\delta_{\infty}} = 2.6 \times 10^5$

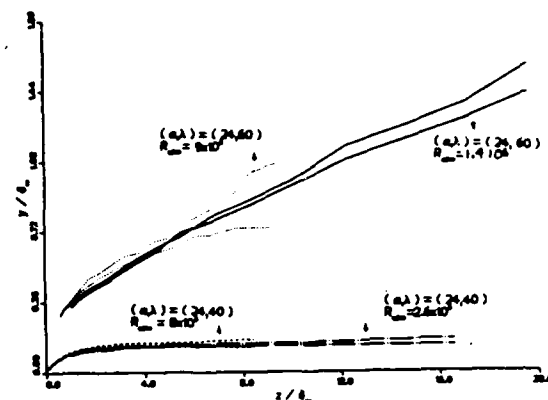


Fig. 26 Height of Surface No. 2 for $(\alpha, \lambda) = (24, 40)$ and $(24, 60)$ deg

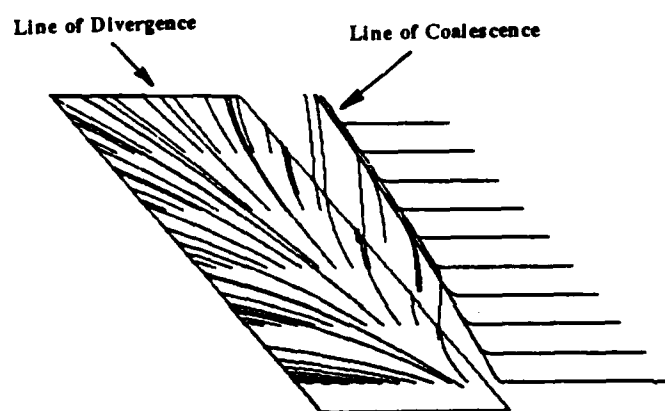


Fig. 24 Computed surface skin friction lines for $Re_{\delta_{\infty}} = 8.1 \times 10^5$

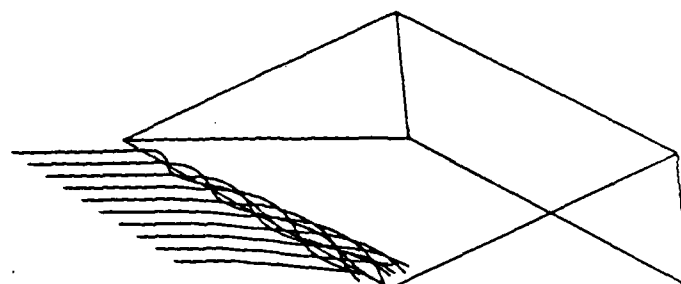


Fig. 27 Streamlines for $(\alpha, \lambda) = (24, 40)$ at $Re_{\delta_{\infty}} = 8.1 \times 10^5$
($y_{start} = 0.02\delta_{\infty}$)

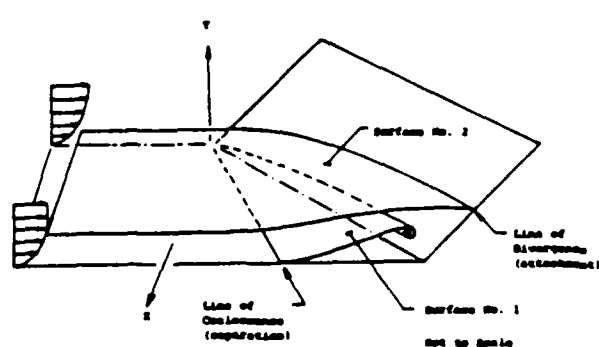


Fig. 25 Flowfield Structure for 3-D Swept Compression Corner

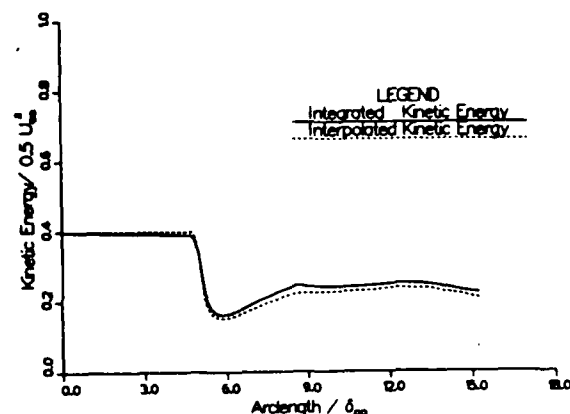


Fig. 28 Integrated and interpolated mean kinetic energy for fifth streamline originating at $y = 0.02\delta_{\infty}$

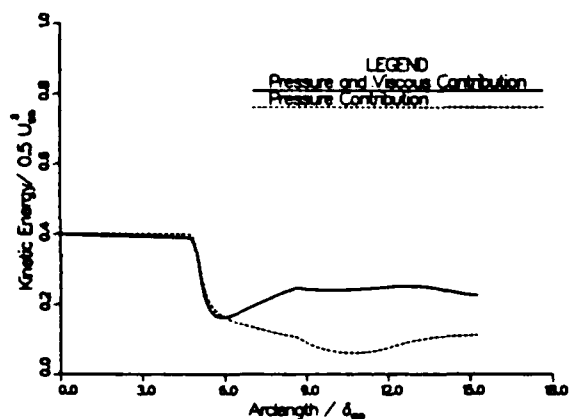


Fig. 29 Pressure plus viscous contribution and Pressure contribution only to mean kinetic energy for fifth streamline originating at $y = 0.025_\infty$

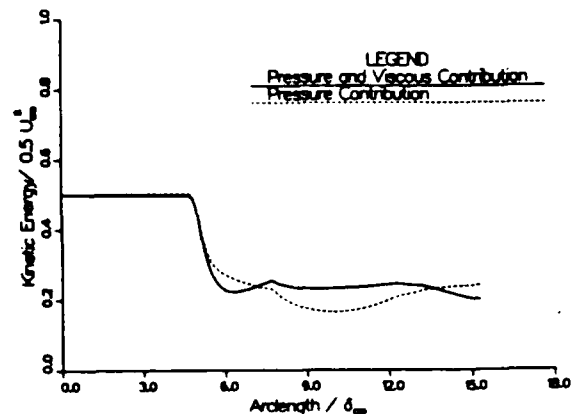


Fig. 32 Pressure plus viscous contribution and Pressure contribution only to mean kinetic energy for fifth streamline originating at $y = 0.05\delta_\infty$

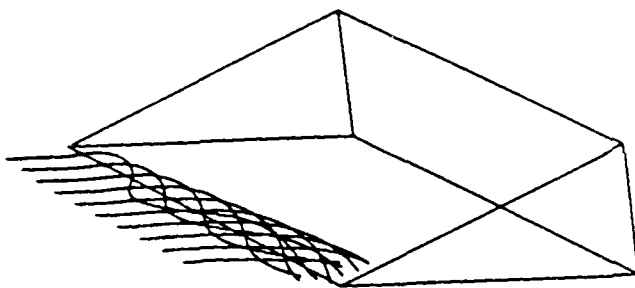


Fig. 30 Streamlines for $(\alpha, \lambda) = (24, 40)$ at $Re_{\delta_\infty} = 8.1 \times 10^5$ ($y_{start} = 0.05\delta_\infty$)

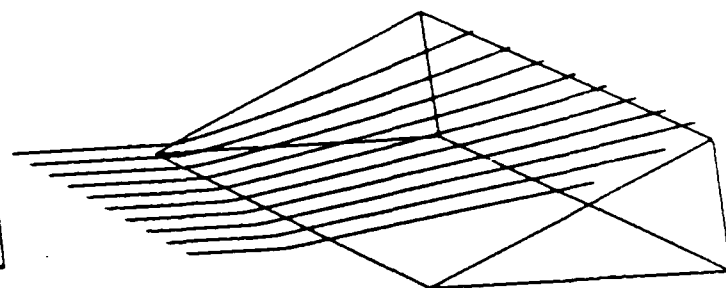


Fig. 33 Streamlines for $(\alpha, \lambda) = (24, 40)$ at $Re_{\delta_\infty} = 8.1 \times 10^5$ ($y_{start} = 0.5\delta_\infty$)

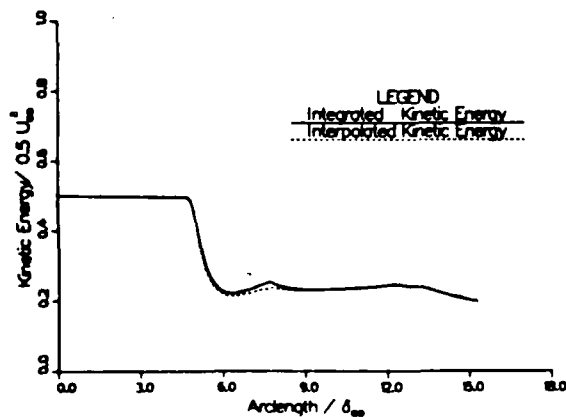


Fig. 31 Integrated and interpolated mean kinetic energy for fifth streamline originating at $y = 0.05\delta_\infty$

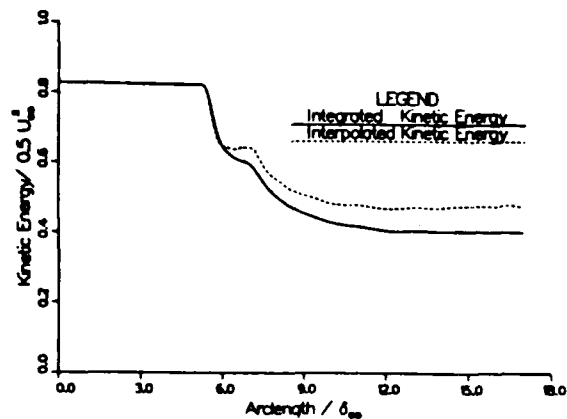


Fig. 34 Integrated and interpolated mean kinetic energy for fifth streamline originating at $y = 0.5\delta_\infty$

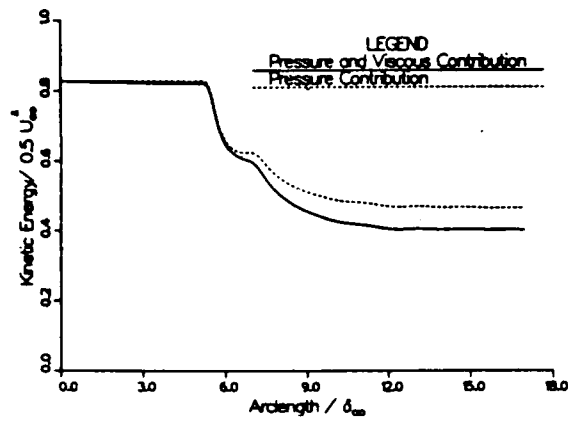


Fig. 35 Pressure plus viscous contribution and Pressure contribution only to mean kinetic energy for fifth streamline originating at $y = 0.5\delta_\infty$

Section VI. Papers

"Numerical Experiments on the 3-D Shock Wave- Boundary Layer Interaction Generated by a Sharp Fin"

by D. Gaitonde and D. Knight

AIAA Paper 88-0309

Presented at the AIAA 26th Aerospace Sciences Meeting
January 11-14, 1988
Reno, NV

Numerical Experiments on the 3-D Shock Wave - Boundary Layer Interaction Generated by a Sharp Fin

D. Gaitonde* and D. Knight**
Department of Mechanical and Aerospace Engineering
Rutgers University
Piscataway, New Jersey 08855

ABSTRACT

A numerical investigation is focussed on the effect of bleed on the three-dimensional shock wave - turbulent boundary layer interaction generated by a 3-D sharp fin with 20° wedge angle at a Reynolds number 9×10^5 based on the upstream boundary layer thickness. The Reynolds-averaged 3-D compressible Navier-Stokes equations in mass averaged variables are solved with the eddy viscosity as prescribed by the Baldwin-Lomax algebraic model. Bleed is applied in the region between the line of upstream influence and the theoretical inviscid shock line in an attempt to reduce or eliminate altogether the undesirable separation observed in such flows. Three magnitudes of mass flux (1%, 2.5% and 5% of free stream) are computed. The computed flow fields are compared with experimental and theoretical results obtained in the absence of bleed. The effect of the described bleed schedule on the flow field is modest and relatively local. Various physical variables such as the pitot pressure and yaw angles are moderately influenced only at close proximity of the surface. In the interaction region, the previously observed overshoot in pitot pressure profile is reduced. Skin friction values increase significantly only in the region of bleed. The line of coalescence is seen to align with the theoretical inviscid shock line though this may be due to the particular region of bleed under consideration. A detailed study of particle pathlines generated from the computed flow field indicates that the effect of bleed is essentially to ingest a portion of the boundary layer. The vortical structure observed in previous research is not significantly affected. The paper also describes results of a numerical investigation of a weak shock-shock intersection in the presence of a turbulent boundary layer. Previous research indicates that such interactions may be capable of producing a given pressure rise with less likelihood of separation than an equivalent strength single shock interaction. Numerical results of flow due to two five degree symmetrically placed wedges on a flat plate are compared with experiment.

1 Introduction

3-D shock wave - turbulent boundary layer interactions (denoted "3-D turbulent interactions") occur in a variety of applications such as aircraft inlets and compressors, wing-body junctures and control surface deflections. In the past few years significant progress has been achieved by theoretical and experimental researchers in the understanding of 3-D turbulent interactions generated by dimensionless geometries such as the sharp fin (Fig. 1) which consists of an unswept wedge at angle of attack α mounted on a flat plate on which develops the incoming turbulent boundary layer.

The principal parameters in such flows are the Mach number M_∞ , the Reynolds number, Re_{δ_∞} , based upon the boundary layer thickness δ_∞ at the streamwise station corresponding to the leading edge of the fin, the thermal boundary conditions and the fin angle α . Experimental results available for such flows may be classified into surface [1, 2, 3, 4, 5, 6] and boundary layer measurements [7, 8, 9, 10, 11]. These experiments cover a range of the above mentioned parameters and have provided valuable insight into the structure of 3-D turbulent interactions.

While a few researchers have achieved success in the analytical treatment of shock - boundary layer interactions especially for weaker shock strengths [12, 13, 14, 15], the thrust of the theoretical effort is mainly numerical. With the advent of high-speed computers, it has become possible to numerically simulate 3-D turbulent interactions [16, 17, 18, 19]. These computations typically employ the Reynolds averaged Navier-Stokes equations coupled with an algebraic [20] or two-equation [21] turbulence model and have demonstrated good agreement with experimental boundary layer and surface measurements at Mach 3 for $Re_{\delta_\infty} = 2.5 \times 10^5$ to 9.0×10^5 and wedge angles up to 20° [10]. Results obtained computationally for the swept-compression corner have also been encouraging [22].

Recent calculations at fin angle 20° by Knight *et al* [10] with two different turbulence models, have proven to be in close agreement with experiment with modest discrepancies in the immediate vicinity of the flat plate. Analysis of these computations has led to the conclusion that the principal flow feature is a large vortical structure aligned with the corner in agreement with the flow field models of Token [23] and Kubota and Stollery [4]. A three-dimensional surface of separation (Fig. 2) emanates from the line of coalescence (separation), and spirals into the vortical center. A second surface, emanating from upstream, intersects the wall at the line of divergence (attachment), and defines the extent of the fluid entrained into the vortical structure.

The characteristics of the above described flow field - specifically the large vortical structure and separated flow - are not ideal in applications such as aircraft inlets. Improvements in the control of high speed 3-D turbulent interactions may lead, therefore, to improved aircraft performance. Several possible means of control may be identified:

- Bleed (suction). Bleed has been traditionally employed in high speed aircraft inlets to prevent boundary layer separation. The effect of suction is to remove the low speed fluid in the boundary layer before it separates from the surface.

*Graduate Student, Student Member AIAA.

**Professor, Associate Fellow AIAA.

- **Blowing:** Experimental measurements by Peake [8] at Mach numbers 2 and 4 and Reynolds number 2×10^5 based on the undisturbed boundary layer thickness indicate that it is possible to control separation by tangential air injection. The theory behind this approach is to supply additional energy to the fluid being retarded in the boundary layer by the pressure rise.
- **Shock-Shock Interaction:** Mee and Stalker [15] have concluded from experimental observations on weak shocks that intersecting shocks can produce a given overall pressure rise with less likelihood of separation than an equivalent strength single shock interaction.
- **Vorticity Distribution Modification:** Since the principal flow feature is a vortical structure, it may be possible to apply control through the introduction of additional vorticity in the longitudinal or spanwise direction.
- **Modification of Geometry:** It may be possible to significantly influence the flow field by minor modifications in the 3-D configuration itself. The effect of raising the fin a slight distance from the flat plate could prove interesting.

The objective of the present research effort is to study these techniques of control through numerical simulation. In this paper the first of these choices, namely bleed (suction), is investigated. The numerical simulation of a weak shock-shock interaction in the presence of a turbulent boundary layer is also described. It is recognized that there is a scarcity of published work describing physical experiments incorporating bleed in 3-D turbulent interactions for the sharp fin configuration and that it is therefore not possible to make direct comparison of the results to be presented with experiment. It may be emphasized, however, that the governing Reynolds averaged 3-D compressible Navier-Stokes equations and the numerical algorithm employed (the hybrid explicit-implicit method of Knight [17]) have been applied successfully to predict turbulent interactions for the 3-D sharp fin [10] and for a simulated 3-D inlet with bleed [24]. In addition, the algebraic turbulent eddy viscosity model of Baldwin and Lomax [20] has been validated for a variety of boundary layer flows [25] with zero, favorable and adverse pressure gradients and in the presence of suction. It is believed therefore that the results presented serve two purposes, namely, to improve the current state of understanding of 3-D turbulent interactions and, to "reduce the required experimental test matrix to the smallest number of configurations [26]" by identifying broad trends should bleed be applied to such flows.

2 Description of computations

2.1 Governing equations and numerical model:

The governing equations are the full mean compressible Navier-Stokes equations using mass averaged variables and strong conservation form. The molecular and turbulent Prandtl numbers are 0.73 and 0.9, respectively.

Turbulence is modeled through the inclusion of the two-layer algebraic turbulent eddy viscosity model of Baldwin and Lomax [20] with the mixing length (ℓ) as specified by the formula of Buleev [27]. The effect of bleed is incorporated in the Van Driest Damping Factor D given by:

$$D = 1 - \exp\left(-\frac{\ell(|\tau_w|\rho_w)^{1/2}N}{26\mu_w}\right) \quad (1)$$

where $|\tau_w|$ is the magnitude of the wall shear stress, μ_w is the wall dynamic viscosity, ρ_w is the fluid density at the wall and N is the bleed correction factor of Cebeci [28] given by

$$N = \exp\left(\frac{5.9}{\mu} \frac{\mu_w \dot{m}}{\sqrt{|\tau_w|\rho_w}}\right) \quad (2)$$

where \dot{m} is the normal mass flux at the wall, with \dot{m} negative for bleed.

A 3-D coordinate transformation is employed as in [10] to facilitate the application of the numerical algorithm and the boundary conditions. The hybrid explicit-implicit algorithm of Knight [24] is employed to solve the governing equations. The implicit algorithm employs Keller's Box Scheme [29] and is applied to the asymptotic form of the Navier-Stokes equations in a thin region adjacent to the solid surfaces. This region, denoted the 'computational sublayer', is defined by $s^{**} \leq 60$, where $s^{**} = s'u_w/\nu_w$, with $u_w = (|\tau_w|/\rho_w)^{1/2}$, τ_w = wall shear stress, and ν_w is the kinematic viscosity at the wall. Typically, the height of this region is less than 1% of the local boundary layer thickness. The asymptotic form of the conservation of momentum, given in [17], represents a balance between convection normal to the surface (associated with bleed), pressure forces and viscous diffusion normal to the surface. The asymptotic form of the conservation of energy [17] is obtained by neglecting the effects of streamwise convection and diffusion and represents a balance between the total enthalpy transported normal to the surface due to convection (associated with the bleed) and viscous diffusion. The explicit algorithm of McCormack [30] is applied to the full Navier-Stokes equations on grid points exterior to the computational sublayer. This includes nearly all of the boundary layer and the external inviscid region. The accuracy of the computational sublayer approach has been verified for 2-D shock wave-turbulent boundary layer interactions in the presence of separation [31], and is examined in Section 2.4 for the present cases.

2.2 Boundary Conditions:

The boundary conditions are (See Fig. 1):

- **Upstream boundary ABHG:** The flow at this boundary is assumed to be 2-D and is generated with a separate code [25] such that the momentum thickness at the leading edge of the fin is in close agreement with experiments of Shapey and Bodgonoff [10]. It is emphasized that these experiments do not incorporate suction. The various flow parameters are indicated in Table 1.
- **Plane of symmetry AFLG:** The normal

component of the velocity and the normal derivatives of the remaining flow quantities are set to zero.

- Right boundary BCDJIH: This boundary is assumed to be sufficiently far from the fin to insure that the boundary layer is locally two-dimensional and therefore a simple gradient boundary condition $\partial/\partial x=0$ is employed.
- Downstream boundary EKJD: The conventional zero gradient condition is specified.
- Fin surface LFKE: Since this is a solid surface, the velocity and the normal pressure gradient are taken to be zero and a fixed surface temperature ($T_w/T_{\text{adiabatic}} = 1.17$) is specified.
- Flat plate ABCDEF: The two components of velocity along the flat plate are specified to be zero. Bleed is applied in the triangular area AYXA shown in Fig. 3. The upstream boundary AX coincides approximately with the line of upstream influence, defined as the line where the incoming flow experiences a 5% increase in static pressure. The downstream boundary, AY, coincides with the theoretical inviscid shock line. Two bleed parameters (abbreviated B.P.) are defined in order to characterize bleed:

$$\text{B.P. I} = \frac{\rho_w v_w}{\rho_\infty u_\infty} \quad (3)$$

where the subscripts w and ∞ denote plate and free stream conditions respectively, u is the free stream velocity of the incoming flow and the v denotes the vertical velocity at the plate. This parameter (B.P. I) directly specifies the mass flux at each grid point in the bleed region. The flux values at the boundaries of the bleed region are ramped up to the full value over typically three grid points to minimize boundary layer effects due to sudden changes in boundary conditions. It is apparent that the suction under consideration may be categorized as porous bleed as opposed to slot bleed.

Since B.P. I does not incorporate the area of bleed and therefore does not adequately describe the total amount being bled off, a second parameter (B.P. II) is defined:

$$\text{B.P. II} = \frac{M}{BL} = \frac{\int_{A_B} (\rho v)_w}{l \int_0^{\delta} \rho(y) u(y) dy} \quad (4)$$

where $l = A_B/\delta_\infty$, M is the total mass bleed rate from the bleed area (A_B) and BL is the mass entering the domain from an equal area of height δ_∞ adjacent to the plate at the upstream boundary. Four cases are computed

categorized by the values of two bleed parameters. These are summarized in Table 2.

	δ_∞ (cm)	M_∞	Re_{δ_∞}	$P_{t,\infty}$ (kPa)	$T_{t,\infty}$ (°K)
Expt.	1.4	2.93	9.8×10^5	690	251
Theory	1.3	2.93	8.8×10^5	690	251

Table 1: Flow Conditions for Experiment and Theory

	B.P. I	B.P. II
Case 1	0.000	0.000
Case 2	0.010	0.011
Case 3	0.025	0.029
Case 4	0.050	0.055

Table 2: Bleed Parameter Values Employed

2.3 Details of Computations:

The computational grid employs 32 streamwise grid planes, uniformly spaced in the x-direction with $\Delta x = \delta_\infty$. The upstream boundary is located at $5\delta_\infty$ upstream of the fin leading edge, and the downstream boundary at $x = 28\delta_\infty$. In the vertical (y) direction, 48 grid points are employed integrating up to approximately $8\delta_\infty$ for Cases 1 and 2 and $8.5\delta_\infty$ for Cases 3 and 4. The number of ordinary points in the spanwise direction in all cases is 32. The sublayer in proximity to the fin is resolved with 8 grid points for all cases while close to the flat plate 8 points are employed for Cases 1 and 2 and 12 points for Cases 3 and 4. This refinement is necessary to adequately resolve all relevant flow features. A complete set of criteria for judging the acceptability of a grid system do not exist at present. A number of necessary criteria established in the literature are presented below.

- Viscous Sublayer: The average height of the first grid point (located within the sublayer) above the boundary should satisfy [24]:

$$z^+ N = \frac{z^+ u_\tau}{\nu_w} N \leq 3 \quad (5)$$

$$u_\tau = \sqrt{\tau_w / \rho_w}$$

and N is the bleed correction factor of Cebeci defined earlier. This requirement is dictated by the use of an algebraic eddy viscosity model (cf. [16, 20]). In the presence of bleed, the height of the first grid point must also satisfy:

$$\frac{z^+ \dot{m}}{\mu_w} < 1 \quad (6)$$

where \dot{m} is the magnitude of bleed imposed at the wall. This requirement arises from an analysis of the sublayer equations in the region near the boundary where $\mu > \epsilon$.

- Height of Sublayer Region: As indicated

earlier, the average height of the sublayer region is restricted to [17, 18]:

$$z'_m \leq 60 \quad (7)$$

where the subscript m denotes the edge of the sublayer.

- Boundary layer: A minimum of fifteen (15) grid points (including sublayer points) are required within the boundary layer [31, 32].

The characteristics of the grids employed for each of cases satisfy all the constraints described above and are presented in Table 3.

Requirement	z^-	z^+N	z_m	z'_m/μ_w	NPBL	
Case 1	Avg.	1.47	1.47	47.41	0.00	16
	Max.	3.03	3.03	97.41	0.00	
Case 2	Avg.	1.47	1.46	50.4	0.30	16
	Max.	3.01	3.01	97.01	0.41	
Case 3	Avg.	0.96	0.94	43.1	0.11	21
	Max.	3.07	3.07	98.8	0.15	
Case 4	Avg.	0.97	0.93	44.88	0.23	21
	Max.	3.05	3.05	136.9	0.3	

Legend: NPBL - Number of Points in Boundary Layer

Table 3: Grid Characteristics

Computations are carried out at the four-pipe CYBER 205 at NASA Ames Research Center. A typical speed of 260 MFLOPS is achieved for the highly vectorized portions of the code. The flow development and required CPU times are provided in Table 4. In this table, T_c is the characteristic time, the time required for a particle at upstream conditions to traverse the length of the computational domain.

Case	T_c	CPU (hours)
1	3.5	4.2
2	4.2	3.6
3	5.1	15.0
4	5.4	17.5

Table 4: Flow Development and CPU hours

2.4 Evaluation of Error Associated with the Sublayer Equations:

The effect of the approximations inherent in the sublayer model are evaluated by integrating the full 3-D boundary layer equations across the sublayer region ($0 \leq z \leq z_m$) to yield the following general expressions for the two components of wall shear stress:

$$r_{ws} = T_{1x} - T_{2x} \quad (8)$$

$$r_{wy} = T_{1y} - T_{2y} \quad (9)$$

$$T_{1x} = \left[v'_m - \frac{\partial p}{\partial x'} \int_0^{z'_m} \frac{z' dz'}{\mu + \epsilon} - \frac{1}{m} \int_0^{z'_m} \frac{v' dz'}{\mu + \epsilon} \right] f(z'_m) \quad (10)$$

$$T_{1y} = \left[v'_m - \frac{\partial p}{\partial y'} \int_0^{z'_m} \frac{z' dz'}{\mu + \epsilon} - \frac{1}{m} \int_0^{z'_m} \frac{v' dz'}{\mu + \epsilon} \right] f(z'_m) \quad (11)$$

$$T_{2x} = \left[\int_0^{z'_m} \frac{1}{\mu + \epsilon} \left\{ (\rho w' - m) u' + \int_0^z \left(\frac{\partial(\rho u'^2)}{\partial x'} + \frac{\partial(\rho u' v')}{\partial y'} \right) dz' \right\} dz' \right] / f(z'_m) \quad (12)$$

$$T_{2y} = \left[\int_0^{z'_m} \frac{1}{\mu + \epsilon} \left\{ (\rho w' - m) v' + \int_0^z \left(\frac{\partial(\rho v'^2)}{\partial y'} + \frac{\partial(\rho v' u')}{\partial x'} \right) dz' \right\} dz' \right] / f(z'_m) \quad (13)$$

$$f(z'_m) = \int_0^{z'_m} \frac{dz'}{\mu + \epsilon} \quad (14)$$

In these equations, the subscript 1 indicates equivalence to the expression employed for r_w in the sublayer model, the subscript 2 indicates the correction to the wall shear stress due to the terms neglected in the sublayer equations and the subscript m indicates the value of the quantity at the edge of the sublayer. The axis z' is normal to the surface and points towards the interior of the domain, the axes x' and y' lie in the plane of the surface and x' , y' and z' form a local right-handed orthogonal coordinate system. The velocities u' , v' and w' are components of the velocity in the x' , y' and z' directions respectively. The quantity m is the bleed mass flow at the solid boundary and is assumed to be orthogonal to it. The error terms in equations (8) and (9) (T_{2x} and T_{2y} respectively) are evaluated with the computed solution. It may be noted that the term $(\rho w' - m)$ is assumed identically zero at all grid points where bleed is applied. An error measure is computed as:

$$\text{Error} = \frac{\sqrt{T_{2x}^2 + T_{2y}^2}}{\sqrt{r_{ws}^2 + r_{wy}^2}} \quad (15)$$

The average error over all solid boundaries in the domain are summarized in Table 5. The error is comparable to the accuracy of many of the experimental measurements, and may be reduced by further grid refinement. It may be noted that the maximum error in skin friction associated with the 2-D sublayer equations applied to 2-D turbulent interactions was observed to be approximately 0.2% [33].

Case	1	2	3	4
Average Error (%)	5.1	5.3	2.4	2.2

Table 3: Average Error Associated With Sublayer Approximation

3 Results

The computed results are evaluated and compared with the boundary layer measurements of Shapey and Bogdonoff 10 and the surface pressure measurements of Goodwin 6. It is emphasized that these experiments did not impose any suction and are presented here to highlight the effects of bleed. In the following discussion, the upstream boundary layer thickness δ_∞ is utilized to scale distances (see [9] for alternative scaling factors for 3-D turbulent interactions), horizontal distances (x_s) are measured relative to the location of the inviscid shock (x_{shock}) at the relevant spanwise position and flow variables are normalized by the value of the variable under free stream conditions unless otherwise mentioned. The experimental stations of Shapey are located as shown in Fig. 3. The coordinates of each location are provided in Table 6.

Survey Location	x_s/δ_∞	z/δ_∞
1	-5.40	5.81
2	-4.40	5.81
3	-3.40	5.81
4	-2.40	5.81
5	-1.40	5.81
6	-0.40	5.81
7	0.60	5.81
8	2.60	5.81
9	3.94	7.81
10	-0.14	4.81
11	1.13	3.81

Legend: $x_s = x - x_{shock}$

Table 6: Survey Locations for the Experiments of Shapey (no bleed)

3.1 Effect of Suction on Flow Variables:

The effect of suction on pitot pressure profiles at Stations 1 and 2, located upstream of the interaction and at the experimentally determined line of upstream influence respectively is negligible. These profiles are similar to those observed in 2-D boundary layer flows. At Station 3 (not shown), located in the vicinity of the line of coalescence, the pitot pressure profiles for Cases 2 to 4 are slightly lower than Case 1 up to about $y/\delta_\infty = 1$ beyond which the profiles match precisely. At Stations 4 (not shown), 5 (Fig. 4) and 6 (not shown), located between the line of coalescence and the theoretical inviscid shock location, the previously observed 10% overshoot is significantly reduced. An approximately 30% reduction in pitot pressure is observed at $y/\delta_\infty = 1$ between Cases 1 and 4 at Station 5. This overshoot is associated with the compression system ahead of the shock wave, the effect of suction on which is discussed later. At Stations 7 (not shown) and 8 (Fig. 5) located immediately downstream of the shock, the numerical

model does not display the prominent overshoot observed experimentally. The slight S-shaped behavior near the plate is more apparent at these stations. It is clear from the pitot pressure profiles presented that the effect of bleed is to increase the pitot pressure modestly up to distances of y/δ_∞ approximately equal to 1. At roughly this distance from the flat plate, the curves cross indicating lower pitot pressure values in the presence of suction for y/δ_∞ greater than approximately 1. The pitot pressure profile at Station 10 (not shown) shows behavior qualitatively similar to that observed at Station 7. The lowest pitot pressure value at Station 10 is overpredicted numerically by about 25% (for the no bleed case) at $y/\delta_\infty = 0.4$. Station 9 displays behavior similar to Station 3 and is not shown.

The effect of suction on the yaw angles is now compared with the experimental data of Shapey. At Stations 1 and 2 (not shown), no effect of suction is observed on the yaw angles which are relatively small. At Station 3 (Fig. 6), significant reduction is observed in the yaw angle in the region up to $y/\delta_\infty < 0.8$. The small negative yaw angle observed for Case 4 is currently under investigation and is thought to be due to the close proximity of this station to a grid point where boundary conditions dictate significant bleed. Stations 4 (not shown) and 5 (Fig. 7) also display modestly lower yaw angles for larger values of bleed. At Station 6 (Fig. 8), a "crossover" of the profiles is observed similar to that observed for pitot pressure. Yaw angles are smaller with higher suction near the flat plate and larger at distances further away. Similar results are observed at Stations 7 through 11 (not shown).

The effect of bleed on the compression system upstream of the shock is more clearly visible in contour plots of static pressure. Figs. 9 through 12 show pressure contours at a streamwise location of $11\delta_\infty$ downstream of the fin leading edge for the four cases respectively. The shock wave is located in the region of most contour density and is clearly visible in the inviscid region. A perceptible increase in the concentration of pressure contours forming the right "leg" of the shock wave is evident leading to the conclusion that suction has the effect of tightening the compression fan. It may be noted that these figures also provide an indication of the extent of shock smearing due to the numerical algorithm.

The computed wall pressure is compared with the experimental data of Goodwin 6 in Fig. 13 in which the surface pressure is plotted against streamwise distance (measured relative to the theoretical inviscid shock location x_{shock}) at a spanwise location of $z/\delta_\infty = 6.9$. This figure indicates that, for the no bleed case, the computations accurately predict the extent of upstream influence and the pressure rise in the interaction region. The effect of bleed is evidently to retard the point of upstream influence slightly in the downstream direction thus reducing moderately the total distance over which the pressure rise is achieved. It may be noted that the experimental data of Hingst and Tanji 34 for 2-D turbulent interactions in the presence of bleed display qualitatively similar effects. The overall pressure rise is not affected in any significant manner. The pronounced drop in wall pressure (Fig. 13) at $x-x_s$ approximately equal to $-4\delta_\infty$ is probably due to relatively large local values of bleed that exist in this region for Cases 3 and 4.

The localized effect of bleed is indicated in the surface skin friction, shown in Fig. 14 at the same location as the data of Goodwin. A steep rise in skin friction is observed in the bleed region with negligible differences elsewhere. The peak values increase with suction. It is apparent that there is a significant drag penalty associated with the employment of suction.

Eddy viscosity values are observed to be generally lower in the presence of bleed. The eddy viscosity at station 5 (normalized by the free stream dynamic viscosity, μ_∞) is plotted in Fig. 15 at Station 5 and shows an approximately 70% drop in value between Cases 1 and 4 at $y/\delta_\infty = 0.4$. Previous research has indicated however, that the details (e.g., velocities, pressures and temperatures) of 3-D turbulent interactions are relatively insensitive to the particular turbulence model employed with the exception of a small fraction of the boundary layer adjacent to the wall.

3.2 Effect of Suction on Flow Field Structure:

The computed solutions are utilized to examine the effect of bleed on the flow structure. Figs. 16 through 19 show computed surface skin friction lines ("surface streamlines") for Cases 1 through 4 respectively. The location of the inviscid shock wave is indicated. It is evident that the lines of coalescence and divergence persist in all cases. The line of coalescence indicates a tendency to align with the shock location in the limiting case. This limiting position is probably dictated by the particular region of bleed under consideration which terminates at the inviscid shock line.

Further investigation of the computed flow fields is carried out with particle tracing methods. A number of particles are released in a systematic fashion at the upstream leading edge of the domain and their motion is numerically integrated. Particles in sets of ten released at two heights above the flat plate are presented to bring out the effects of suction on flow structure. Two views are shown for each case and each height - a top view and a view looking downstream. The flat plate is outlined in each figure for clarity.

Figs. 20 through 23 show traces of particles released at a height of $y/\delta_\infty = 0.1$. Particles for Cases 1 and 2 enter the vortical structure with no obvious differences. For Case 3 on the other hand, whereas particles closer to the fin enter the vortex, those away from the fin are in fact ingested into the flat plate. This ingestion is even more apparent for Case 4 where the bleed is highest and all but one particle - that closest to the fin - are ingested. It may be mentioned that near the corner formed by the fin leading edge and the flat plate, the particle traces may be inaccurate due to the large gradients present. It is clear that with increase in suction a larger portion of the boundary layer is ingested as may be expected.

Higher into the boundary layer, all cases display the prominent vortical structure mentioned previously. Figs. 24 through 27 show traces of particles released at $y/\delta_\infty = 0.5$. For all cases, particles nearer the fin are swept underneath those further away. The particles rotate counterclockwise when viewed in the downstream direction. It is apparent that the effect of bleed on the shape and dimension of the vortical structure is negligible. This is more obvious in Fig. 28 where the

trace of a single particle (originating at a spanwise distance of $5\delta_\infty$ and a vertical distance of $0.5\delta_\infty$ above the flat plate) is shown for all cases. At this distance above the flat plate ($y/\delta_\infty = 0.5$), the yaw angle profiles discussed previously (see Figs. 6 through 8) display modestly lower values in the presence of bleed. The particle traces in Fig. 28 are therefore consistent with the yaw angles presented previously.

It is clear that the mean flow field pattern is dominated by the large vortical structure even in the presence of strong bleed. The effect of bleed is to simply ingest a larger portion of the boundary layer for larger suction values.

4 Weak Shock-Shock Intersection in the Presence of a Turbulent Boundary Layer

Mee [35] and Mee and Stalker [15] describe several experiments with weak shock-shock intersection in the presence of a turbulent boundary layer. They conclude that "intersecting shock interactions can produce a given overall pressure rise with less likelihood of separation than an equivalent strength single shock interaction". As a benchmark, the flow past two 5° fins mounted on a flat plate (Fig. 29) is computed and compared with experiment. The governing equations and numerical model are as described in Section 2.1. The flow parameters are:

$$\begin{aligned} M_\infty &= 1.85 \\ \delta_\infty &= 1.9 \text{ (mm)} \\ Re &= 4.1 \cdot 10^7 \text{ (m}^{-1}\text{)} \\ P_{t_\infty} &= 300 \text{ (kPa)} \\ T_{t_\infty} &= 295 \text{ (K)} \end{aligned}$$

δ_{av} is the average boundary layer thickness in the experimental measurement region [15]. Since line EF (Fig. 29) is a line of symmetry, the flow in the half area ABFE is computed. The flow in EFCD is then constructed by symmetry considerations. On the fin and plate surfaces, solid boundary conditions are applied (see fin surface in Section 2.2). At the upstream boundary, the flow is assumed to be 2-D and as for the bleed cases, the flow variables are generated with a separate 2-D code by matching the average boundary layer thickness with that published in the experiments of Mee and Stalker. Zero gradient extrapolation is employed at the downstream boundary and symmetry boundary conditions are applied on the symmetry boundaries. The grid employs forty (40) streamwise grid planes, uniformly spaced in the x-direction with $\Delta x = \delta_{av}$. The upstream boundary is located $4\delta_{av}$ upstream of the fin leading edge, and the downstream boundary is at $35\delta_{av}$ downstream. Forty eight (48) and thirty two (32) grid points are respectively employed in the vertical (y) and spanwise (z) directions. Both the fin and plate sublayers are resolved with eight (8) points each. All grid constraints described in Section 2.3 are satisfied and details are omitted for the sake of brevity. Convergence is achieved at a flow development time of $5.2 T_c$ (see Section 2.3) corresponding to a CPU requirement of 5.5 hours on the CYBER 205.

The available experimental results 35 consist of surface pressure measurements in the interaction region and limiting streamline patterns recorded with the china film

technique. Fig. 30 shows numerical pressure contours on the flat plate. The quantity plotted in this figure is the pressure rise above its upstream value normalized with the theoretical inviscid pressure rise due to the first shock wave. The experimental surface pressure contour plot is shown in Fig. 31 and corresponds to the area marked AHXY in Fig. 30. A comparison of the two figures reveals differences in the extent of upstream influence of the interaction and the rate of pressure rise. The computations predict a larger upstream influence than observed in experiment. This is in contrast to results published previously [10] where, for stronger (single shock) interactions at higher Mach and Reynolds numbers, computations with two different eddy viscosity models both underpredicted the extent of upstream influence. In the present instance, if the upstream influence is measured as the distance normal to the shock wave where the pressure rises by 10% of the final pressure rise after the first shock, the computed upstream influence distance is approximately 13% larger. The computed surface pressure also increases at a steeper rate after the initial pressure rise. Fig. 32 shows computed surface streamlines and may be compared with those obtained experimentally (Fig. 33). The resemblance of the two patterns - numerical and experimental - to each other is clearly evident. As expected for such weak interactions, there is no line of coalescence. Further analysis of the computed flow field indicates the absence of separation (as expected). Fig. 34 shows traces of particles released at 0.1 and 0.3 δ_{99} above the flat plate respectively.

5 Conclusions and Future Work

A computational study of the effect of bleed on the 3-D shock wave turbulent boundary layer interaction generated by a sharp fin at Mach 3 for fin angle $\alpha = 20^\circ$ and $Re_{\delta_{99}} = 9 \times 10^6$ indicates remarkably modest influence of suction. The effect of bleed is to cause a tightening of the compression system ahead of the shock wave. The overshoot observed in pitot pressure profiles due to the compression system ahead of the shock is significantly reduced. There is a tendency of the line of coalescence to align with the downstream boundary of bleed although this statement is probably valid only for the bleed region under present consideration. The computations indicate that the particular bleed schedule described is incapable of controlling or significantly modifying the undesirable separation and large vortical structure observed in previous research.

Results from a numerical simulation of a weak shock-shock intersection in the presence of a turbulent boundary layer show overall good agreement with available experimental data. Current research efforts are focussed on:

1. Bleed behind shock: For completeness, the effect of 1% bleed applied in the area between the fin and the theoretical inviscid shock wave is being investigated.
2. Shock-Shock Interactions: It is proposed to examine the flow structure due to a strong shock-shock intersection in the presence of a turbulent boundary layer. The precise parameters to be employed are currently being determined in conjunction with the Princeton Gas Dynamics Laboratory.

ACKNOWLEDGEMENTS

This research was sponsored by the Air Force Office of Scientific Research under AF Grant # 86-0266 monitored by Dr. James Wilson. The authors would like to thank Dr. C.C. Horstman for many helpful discussions. The assistance of the staff at the Ames Research Center is gratefully acknowledged.

References

- [1] Stanbrook, A.
An Experimental Study of the Glancing Interaction Between a Shock Wave and a Boundary Layer. In *British ARC CP-555*. July, 1960.
- [2] McCabe, A.
The Three-Dimensional Interaction of a Shock-Wave with a Turbulent Boundary Layer. *The Aeronautical Quarterly* 17:231-252, 1966.
- [3] Law, C.
Three-Dimensional Shock Wave/Turbulent Boundary Layer Interactions at Mach 6. Technical Report TR-75-0191, ARL, 1975.
- [4] Kubota, H. and Stollery, J.
An Experimental Study of the Interaction Between a Glancing Shock Wave and a Turbulent Boundary Layer. *J. Fluid Mech.* 116:431-458, 1982.
- [5] Dolling, D. and Bogdonoff, S.M.
Upstream Influence in Sharp Fin Induced Shock Wave Turbulent Boundary-Layer Interactions. *AIAA Journal* 21:143-145, January, 1983.
- [6] Goodwin, S.
An Exploratory Investigation of Sharp-Fin Induced Shock Wave/Turbulent Boundary Layer Interactions at High Strengths. Master's thesis, Princeton University, 1984.
- [7] Oskam, B., Vas, I. and Bogdonoff, S.
An Experimental Study of 3-D Flowfields in an Axial Corner at Mach 3. *AIAA Paper 77-689*, 1977.
- [8] Peake, D.
Three-Dimensional Swept Shock/Turbulent Boundary Layer Separations with Control by Air Injection. Technical Report Aero. Report No. LR-592, National Research Council - Canada, 1976.
- [9] McClure, W. and Dolling, D.
Flowfield Scaling in Sharp Fin-Induced Shock Wave Turbulent Boundary Layer Interaction. *AIAA Paper 83-1754*, 1983.
- [10] Knight, D., Horstman, C., Shapey, B. and Bogdonoff, S.
The Flowfield Structure of the 3-D Shock Wave - Boundary Layer Interaction Generated by a 20 Deg. Sharp Fin at Mach 3. *AIAA Paper 86-0343*; to appear. *AIAA Journal*, 1986.
- [11] Holden, M.
Experimental Studies of Quasi-Two Dimensional and Three-Dimensional Viscous Interaction Regions Induced by Skewed-Shock and Swept-Shock Boundary Layer Interactions.

- AIAA Paper 84-1677*, 1984.
- 12 Inger, G.
Supersonic Viscous-Inviscid Interaction of a Swept Ramp with a Turbulent Boundary Layer.
AIAA Paper 85-1669, 1985.
 - 13 Inger, G.
Incipient Separation and Similitude Properties of Swept Shock/Turbulent Boundary Layer Interactions.
AIAA Paper 86-0345, 1986.
 - 14 Stalker, R.
Spanwise Propagation of Disturbances in Swept Shock Wave - Boundary Layer Interactions.
AIAA Paper 82-0988, 1982.
 - 15 Mee, D. and Stalker, R.
Investigation of Weak Shock-Shock and Shock-Expansion Intersection in the Presence of a Turbulent Boundary Layer.
AIAA Paper 87-0549, 1987.
 - 16 Horstman, C. and Hung, C.
Computation of Three-Dimensional Turbulent Separated Flows at Supersonic Speeds.
AIAA Paper 79-0002, 1979.
 - 17 Knight, D.D.
A Hybrid Explicit-Implicit Numerical Algorithm for the Three-Dimensional Compressible Navier-Stokes Equations.
AIAA Journal 22:1056-1063, August, 1984.
 - 18 Knight, D.D.
Calculation of Three Dimensional Shock/Turbulent Boundary Layer Interaction.
AIAA Journal 12:1885-1893, December, 1985.
 - 19 Knight, D.D.
Modelling of Three-Dimensional Shock Wave Turbulent Boundary Layer Interactions.
Macroscopic Modelling of Turbulent Flows, Lecture Notes in Physics, 230, Springer-Verlag, pp. 177-201, 1985.
 - 20 Baldwin, B. and Lomax, H.
Thin Layer Approximation and Algebraic Model for Separated Flows.
AIAA Paper 78-257, 1978.
 - 21 Jones, W. and Launder, B.
The Prediction of Laminarization with a Two-Equation Model of Turbulence.
Int. J. Heat and Mass Transfer 15:301-304, 1972.
 - 22 Knight, D., Horstman, C., Ruderich, R., Mao, M.-F. and Bogdonoff, S.
Supersonic Turbulent Flow Past a 3-D Swept Compression Corner at Mach 3.
AIAA Paper 87-0551, 1987.
 - 23 Token, K.
Heat Transfer Due to Shock Wave Turbulent Boundary Layer Interactions in High Speed Weapons Systems.
Technical Report TR-74-77, AFFDL, 1974.
 - 24 Knight, D.D.
Calculation of a Simulated 3-D High Speed Inlet using the Navier-Stokes Equations
AIAA Paper 83-1165, 1983.
 - 25 York, B.
Evaluation of the Baldwin-Lomax Turbulence Model for a Class of Boundary Layer Flows.
Master's thesis, Rutgers University, 1984.
 - 26 Paynter, G.
Current Status of Inlet Flow Prediction Methods. In *12th U.S. Navy Symposium on Aeroballistics.* David Taylor Naval Ship Research and Development Center, Bethesda, Maryland, May, 1982.
 - 27 Buleev, N.
Theoretical Model of the Mechanism of Turbulent Exchange in Fluid Flows.
Technical Report 957, AERE, Hartnell, England, 1963.
 - 28 Cebeci, T. and Smith, A.M.O.
Analysis of Turbulent Boundary Layers.
Academic Press, 1974.
 - 29 Keller, H.
Accurate Difference Methods for Nonlinear Two-Point Boundary Value Problems.
Siam J. Numerical Analysis 11:305-320, 1974.
 - 30 MacCormack, R.
Numerical Solution of the Interaction of a Shock Wave with a Laminar Boundary Layer.
Lecture Notes in Physics, Vol. 8 Springer-Verlag, pp. 151-163, 1971.
 - 31 Knight, D.D.
Improved Calculation of High Speed Inlet Flows - Part I: Numerical Algorithm.
AIAA Journal 19:34-41, January, 1981.
 - 32 Knight, D.D.
Improved Calculation of High Speed Inlet Flows - Part II: Results.
AIAA Journal 19:172-179, February, 1981.
 - 33 Knight, D.D.
A Hybrid Explicit - Implicit Numerical Algorithm for the Three - Dimensional Compressible Navier-Stokes Equations.
AIAA Paper 83-0223, 1983.
 - 34 Hingst, W.R. and Tanji, F.T.
Experimental Investigation of Two-Dimensional Shock-Turbulent Boundary Layer Interactions with Bleed.
Technical Report 83057 (AIAA 83-0135), NASA, 1983.
 - 35 Mee, D.J.
Experiments Involving the Interactions of a Turbulent Boundary Layer with Single and Intersecting Fin-Induced Swept Shock Waves and Swept Expansion Fans.
Technical Report 11 86, Department of Mechanical Engineering, University of Queensland, Australia, 1986.

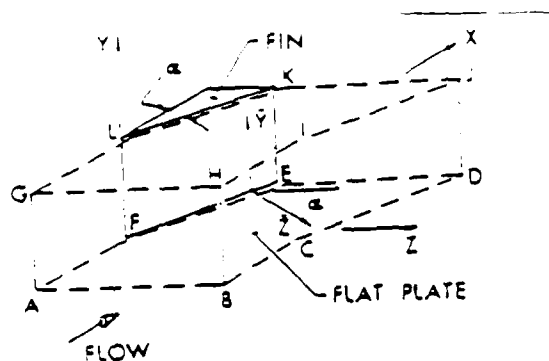


Figure 1: Physical Region for the 3-D Sharp Fin

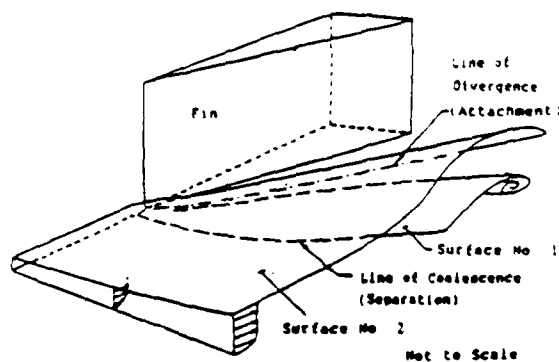
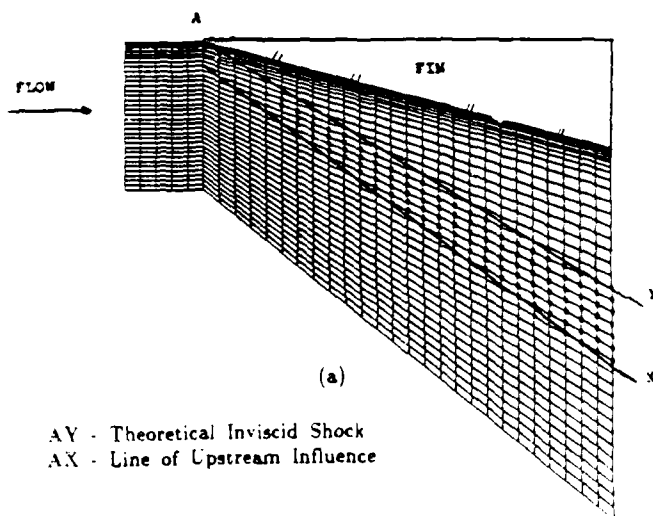


Figure 2: Mean Flow Field Structure



AY - Theoretical Inviscid Shock
AX - Line of Upstream Influence

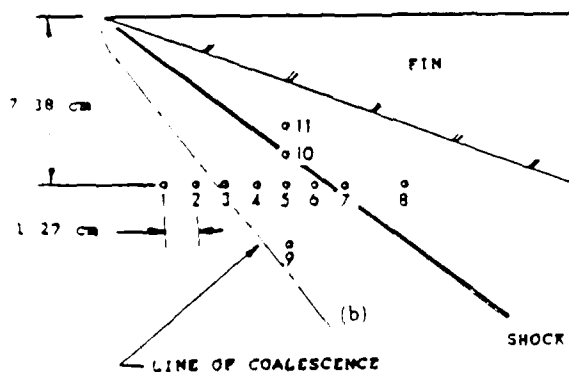


Figure 3: Bleed Region and Location of Experimental Stations

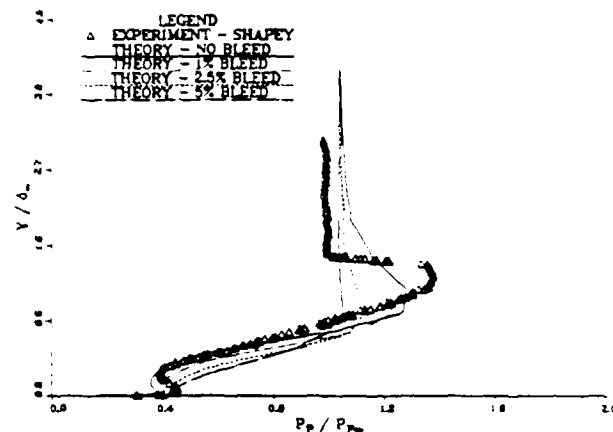


Figure 4: Pitot Pressure at Station 5

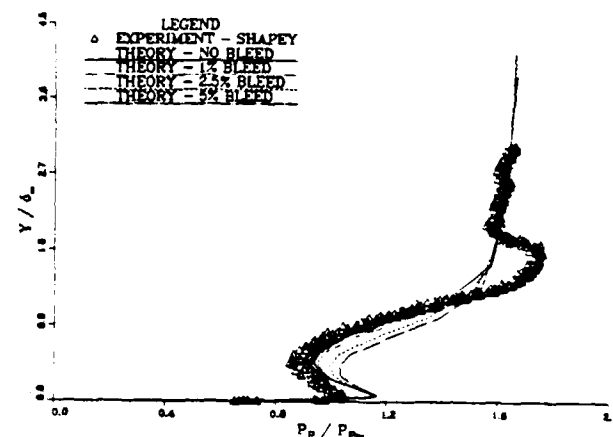


Figure 5: Pitot Pressure at Station 8

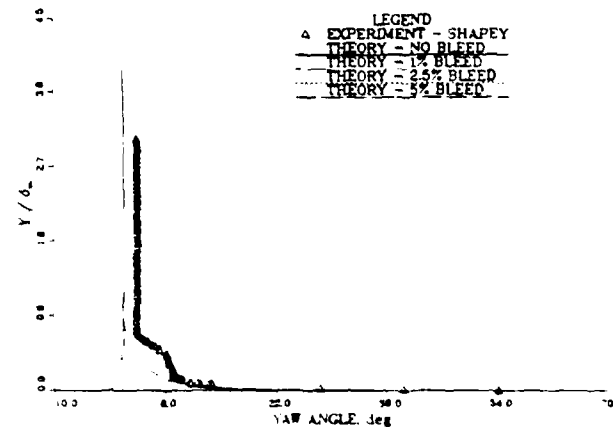


Figure 6: Yaw Angles at Station 3

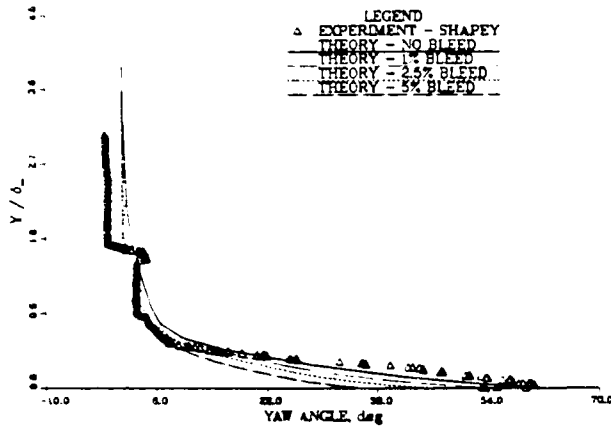


Figure 7: Yaw Angles at Station 5

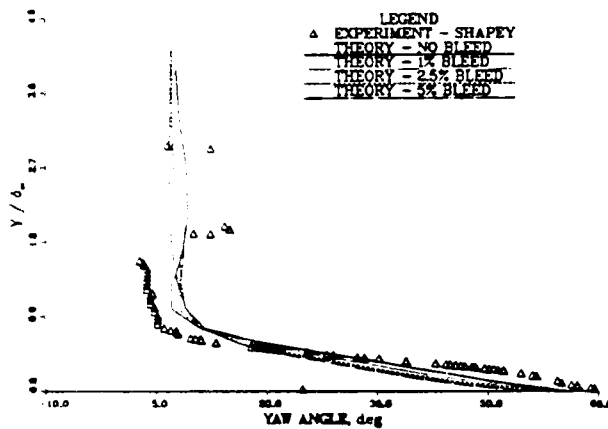


Figure 8: Yaw Angles at Station 6

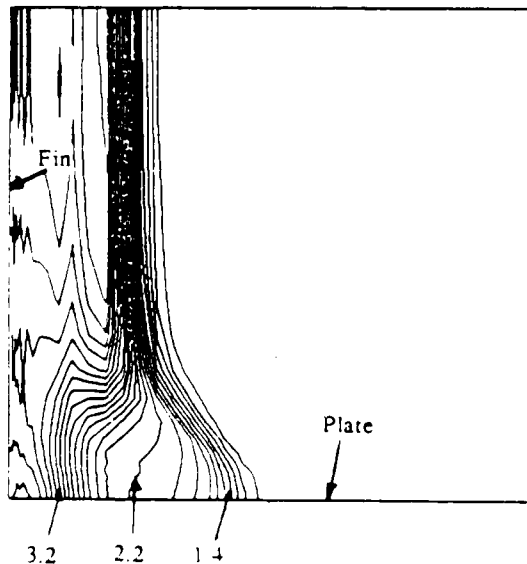


Figure 9: Computed Static Pressure ($P/P_{\infty, \text{upstream}}$) Contours at $x = 11 \delta_{\infty}$ from Fin Leading Edge - Case 1

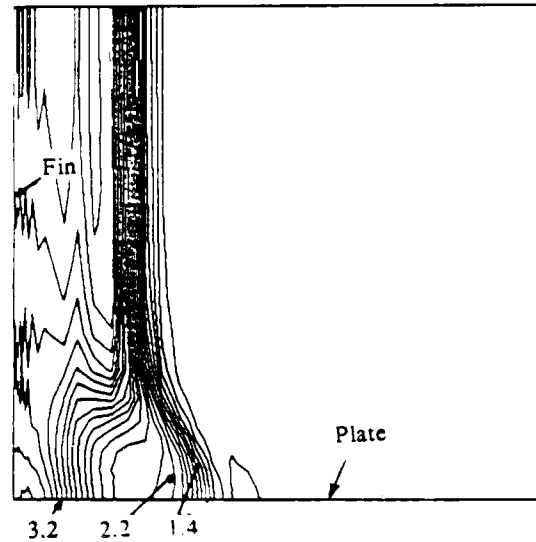


Figure 10: Computed Static Pressure ($P/P_{\infty, \text{upstream}}$) Contours at $x = 11 \delta_{\infty}$ from Fin Leading Edge - Case 2

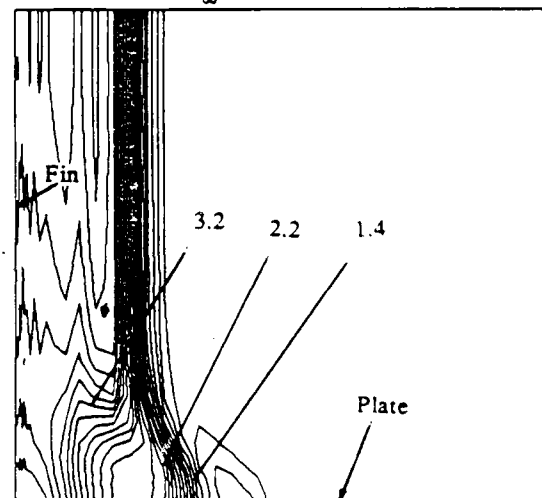


Figure 11: Computed Static Pressure ($P/P_{\infty, \text{upstream}}$) Contours at $x = 11 \delta_{\infty}$ from Fin Leading Edge - Case 3

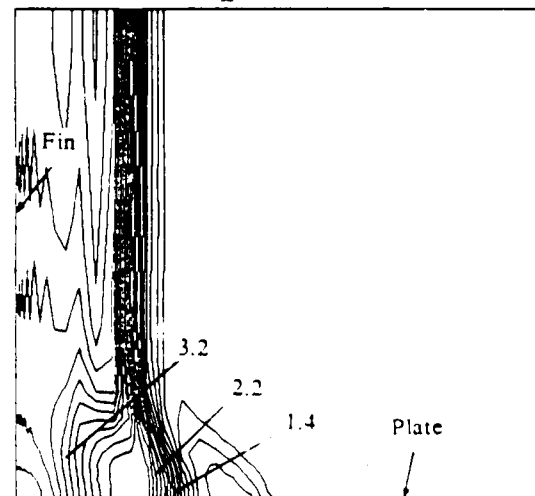


Figure 12: Computed Static Pressure ($P/P_{\infty, \text{upstream}}$) Contours at $x = 11 \delta_{\infty}$ from Fin Leading Edge - Case 4

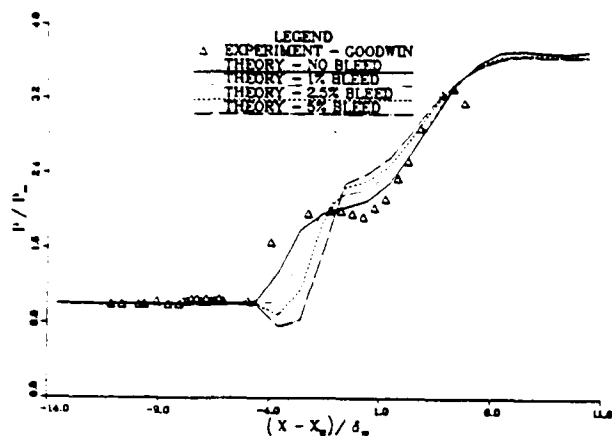


Figure 13: Surface Pressure Profiles at $z/\delta_\infty = 6.9$

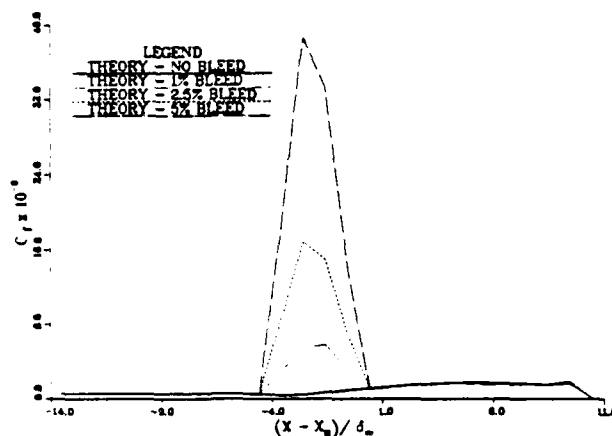


Figure 14: Skin Friction Profiles at $z/\delta_\infty = 6.9$

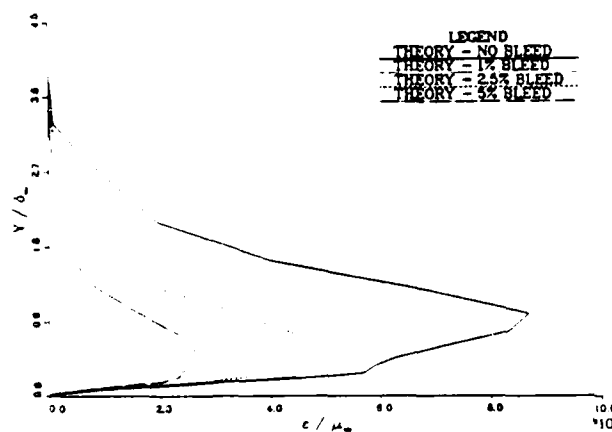


Figure 15: Computed Eddy Viscosity Values at Station 5

Theoretical Inviscid Shock

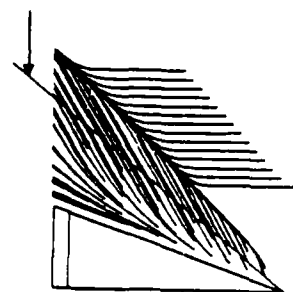


Figure 16: Surface Skin Friction Lines - Case 1

Theoretical Inviscid Shock

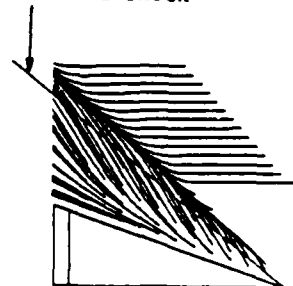


Figure 17: Surface Skin Friction Lines - Case 2

Theoretical Inviscid Shock

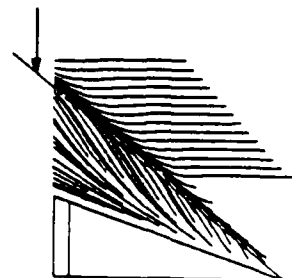


Figure 18: Surface Skin Friction Lines - Case 3

Theoretical Inviscid Shock

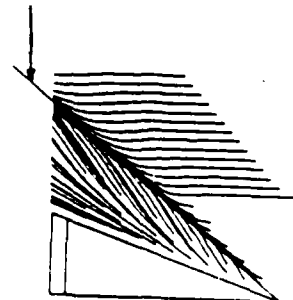


Figure 19: Surface Skin Friction Lines - Case 4

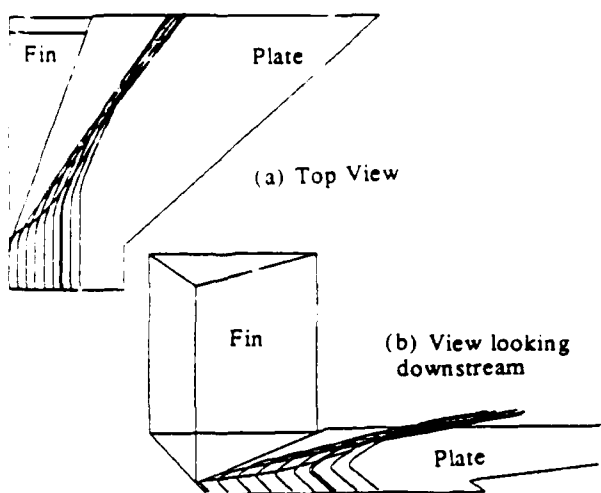


Figure 20: Traces of Particles Released at $y/\delta_\infty = 0.1$
- Case 1

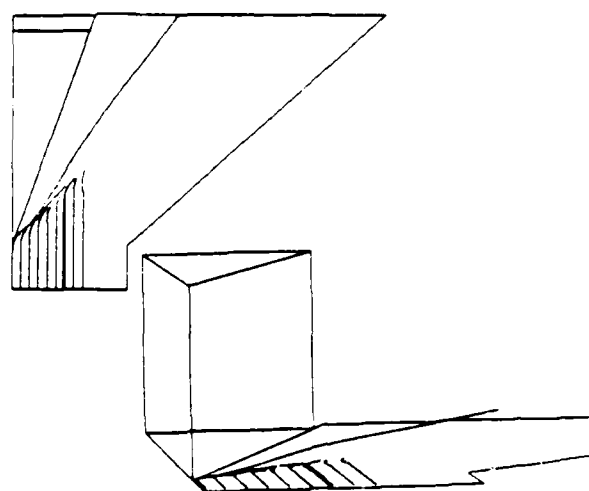


Figure 23: Traces of Particles Released at $y/\delta_\infty = 0.1$
- Case 4

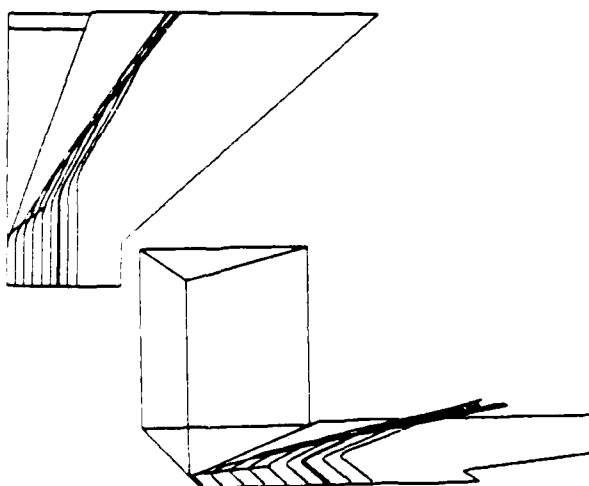


Figure 21: Traces of Particles Released at $y/\delta_\infty = 0.1$
- Case 2

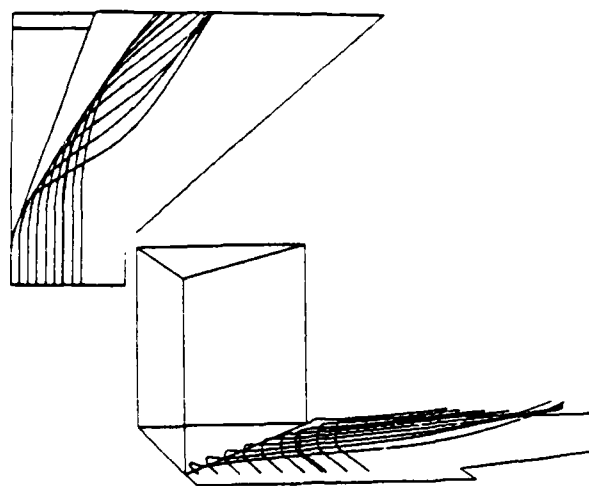


Figure 24: Traces of Particles Released at $y/\delta_\infty = 0.5$
- Case 1

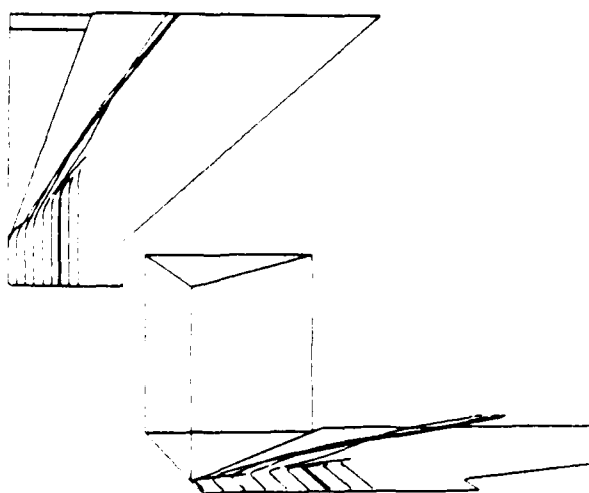


Figure 22: Traces of Particles Released at $y/\delta_\infty = 0.1$
- Case 3

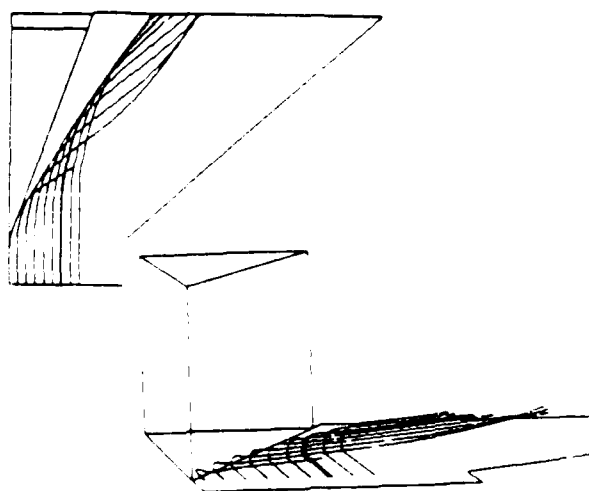


Figure 25: Traces of Particles Released at $y/\delta_\infty = 0.5$
- Case 2

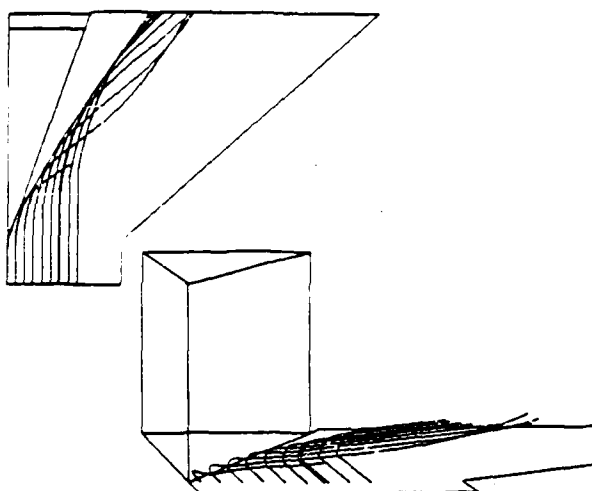


Figure 26: Traces of Particles Released at $y/d_{\infty} = 0.5$
- Case 3

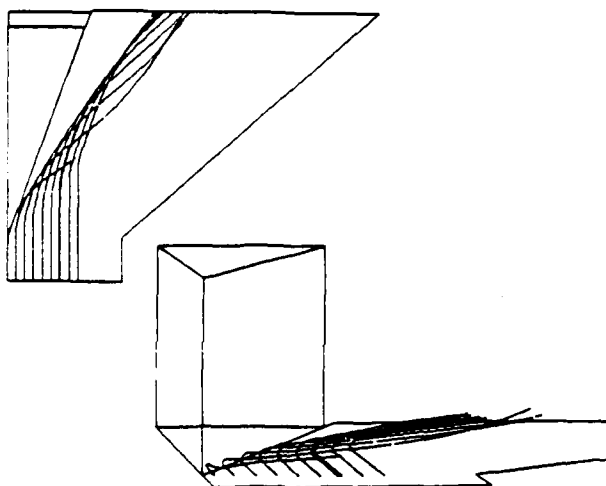


Figure 27: Traces of Particles Released at $y/d_{\infty} = 0.5$
- Case 4

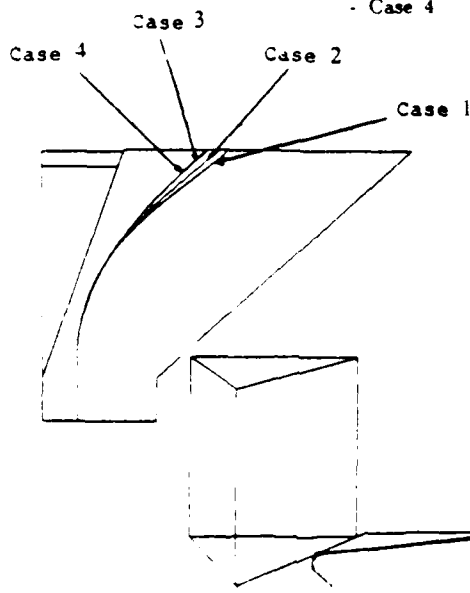


Figure 28: Traces of Single Particle Released at $y/d_{\infty} = 0.5$ and $z/d_{\infty} = 0.0$ - All Cases

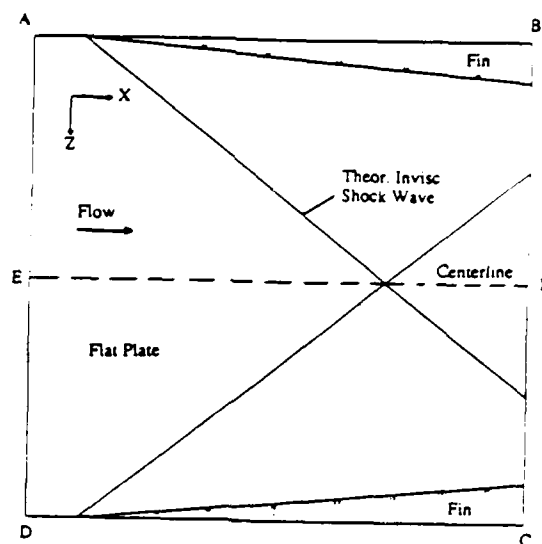


Figure 29: Geometry for Intersecting Shocks Interaction - Top View

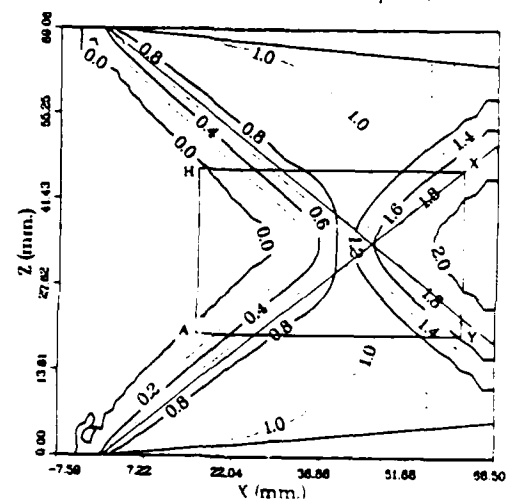


Figure 30: Pressure on Flat Plate - Computation

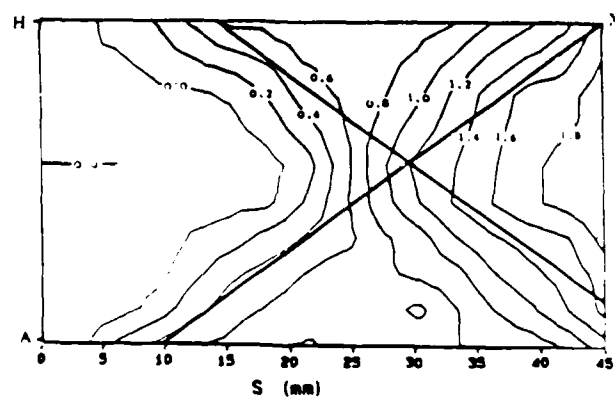


Figure 31: Pressure on Flat Plate - Experiment
From 35

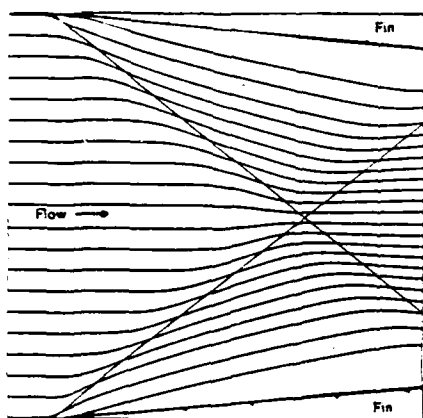


Figure 32: Limiting Surface Streamlines on Flat Plate
- Computation

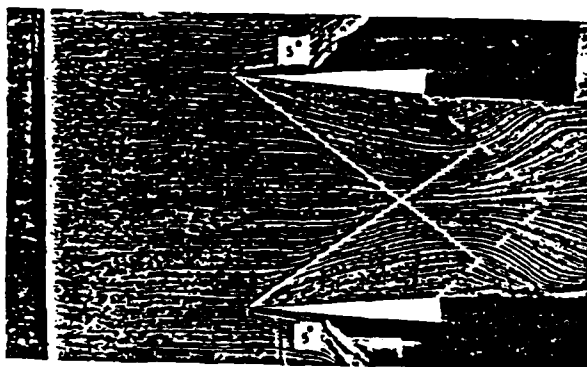
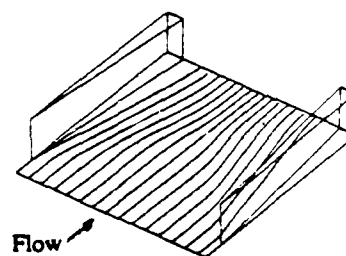
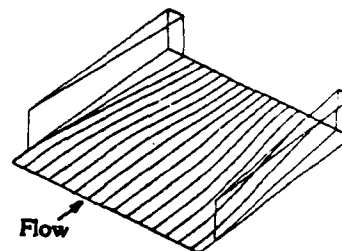


Figure 33: Limiting Surface Streamlines on Flat Plate
- Experiment. From [35]



a) $y \quad \delta_{av} = 0.1$



b) $y \quad \delta_{av} = 0.3$

Figure 34: Traces of Particles Released at 0.1 and
0.3 δ_{av}

END

DATE

FILMED

5-88

DTIC